Title

Exploring CO2 reduction and crossover in membrane electrode assemblies

Journal

Nature Chemical Engineering, 1(5)

ISSN

2948-1198

Authors

Lees, Eric W

Bui, Justin C

Romiluyi, Oyinkansola

et al.

Publication Date

2024-05-01

DOI

10.1038/s44286-024-00062-0

Peer reviewed

Exploring CO_2 reduction and crossover in membrane-electrode assemblies

Eric W. Lees[1], Justin C. Bui[2], Oyinkansola Romiluyi[1,2], Alexis T. Bell[2], & Adam Z. Weber[1]*

[1] Energy Technologies Area
Lawrence Berkeley National Laboratory
Berkeley, CA 94720, USA

[2] Department of Chemical and Biomolecular Engineering
University of California Berkeley
Berkeley, CA 94720, USA

Corresponding Author: azweber@lbl.gov

Electrochemical CO_2 reduction (CO2R) using renewable electricity is a key pathway towards synthesizing fuels and chemicals. In this study, multi-physics modeling is used to interpret obtained experimental data for CO2R to CO using Ag catalysts in a membrane-electrode assembly. The 1-D model is validated using measured CO_2 crossover and product formation rates. The kinetics of CO formation are described by Marcus-Hush-Chidsey kinetics, which enables accurate prediction of the experimental data by accounting for the reorganization of the solvent during CO2R. The results show how performance is dictated by competing phenomena including ion formation and transport, CO_2 solubility, and water management. The model shows that increasing the ion-exchange capacity of the membrane and surface area of the catalyst increases CO formation rates by >100 mA cm^{-2} without negatively impacting CO_2 utilization. This study provides insights into how to manage the trade-off between productivity and CO_2 utilization in CO2R electrolyzers.

1. Introduction

Electrochemical CO_2 reduction (CO2R) can be used to convert CO_2 emitted from various stationary sources into valuable chemicals and fuels. Carbon monoxide (CO) is a valuable product of CO2R because of its utility as a reactant for the production of longer chain hydrocarbons *via* Fischer-Tropsch synthesis.[1] Technoeconomic analyses of CO2R show that CO can be produced for as little as \$0.6-1.0 kg^{-1} [2]; however, CO produced by steam reforming of natural gas currently costs ~\$0.15 kg^{-1} [3]. The key to overcoming this price differential and making a CO2R electrolyzer economical is to minimize the energy costs by maximizing the partial current density for the CO-evolution reaction (i_{COER}) while minimizing the cell voltage (V_{cell})[4,5].

Membrane-electrode assemblies (MEAs) are the most efficient CO_2 electrolyzer architectures for high rates of CO formation[6]. MEA devices for CO2R are similar in construction to water electrolyzers and hydrogen fuel cells, consisting of porous electrodes separated by a thin-ion-exchange membrane. The use of an anion-exchange membrane (AEM), a type of ion-exchange membrane composed of a polymer with fixed positive charges (typically quaternary amines), has been shown to enable high CO formation rates (i_{CO} > 200 mA cm^{-2}) in CO2R electrolyzers[7]. However, AEMs also permit the crossover of (bi)carbonate anions (*i.e.*, HCO_3^- and CO_3^{2-}) from the cathode to the anode, where the (bi)carbonate anions are converted by a pH-swing to reform CO_2, which is lost from the anode[8]. The CO_2 crossover rate is therefore another figure-of-merit that must be considered when designing a CO2R electrolyzer because it represents an efficiency loss that defines the costs associated with separating and recycling the CO_2 reactant downstream

of the electrolyzer[9, 10]. Cation-exchange membranes and bipolar membranes can decrease the rate of CO_2 crossover in CO2R electrolyzers by delivering protons to the cathode that convert (bi)carbonates back into CO_2 before they cross the membrane.[11, 12] However, these membranes yield lower CO partial current densities because of the acidic conditions furnished at the cathode, which promotes HER.[13]

While the development of membranes and electrodes tailored for CO2R is an active field,[14] relatively few theoretical studies have investigated how the properties of the materials used in electrolyzers impact the rate of CO2R in an MEA, and even fewer studies combine self-consistent experimental and theoretical studies. Several models of MEAs for CO2R exist that examine the physics of CO_2 transport[15, 16, 17, 18]. However, these models do not adequately account for the chemistry occurring at the anode, in the anolyte, and in the membrane adjacent to the cathode, all of which impact the performance of an MEA. Consequently, these models cannot accurately reproduce experimental polarization and CO_2 crossover measurements simultaneously. More sophisticated continuum models that correlate the performance of CO2R MEAs with material properties and operating conditions are therefore required to resolve the mechanisms of transport losses and optimize the properties of the membrane, catalyst layer, and electrolyte. Of particular importance are coupled phenomena such as electroosmosis and water management in general, something often neglected in CO2R studies that focus mainly on new materials.

In this study, we conduct experimental investigations of CO2R to form CO on Ag in MEA cells and use the crossover and partial-current-density data to inform and validate the development of a continuum 1D multi-physics cell model. The model is then used to explore the

effects of the thickness and electrochemically active surface area of the catalyst layer, the ion-exchange capacity (IEC) of the membrane, and the anolyte concentration on CO2R performance metrics. The model accurately predicts the crossover of CO_2 from cathode to and anode and enables correlation of the charge-carrying species with the rate of CO_2 crossover and fluxes of water in the MEA. Key to predicting the rate of CO2R at high overpotentials is the adoption of Marcus-Hush-Chidsey (MHC) theory (which accounts for the reorganization of solvent molecules during electron transfer) as opposed to traditional Tafel kinetics. The experimentally-validated model utilizes chemical-engineering fundamentals that guide the design of next-generation CO2R electrolyzers.

2. Results and discussion

2.1 Model development, validation, and comparison of MHC and Tafel kinetics for COER

A 1-D isothermal continuum model was developed in COMSOL Multiphysics 6.0 to simulate the partial current densities for H_2, CO_2, and O_2 formation in a CO2R electrolyzer MEA and the crossover of carbon from cathode to anode (**Figure 1a, b**). The model consists of five domains: a platinized titanium anode porous-transport layer (thickness = 190 μm), an iridium-oxide anode catalyst layer (10 μm), an ion-exchange membrane (50 μm), a cathode catalyst layer (10 μm) composed of silver nanoparticles on carbon mixed with ionomer, and a cathode gas-diffusion layer (GDL; 325 μm; **Figure 1c**). Volume-averaged properties for each phase are used

as inputs to solve the conservation equations for momentum, mass, and charge transport (full model description in **Methods**). Model parameters are shown in **Table S1-S6**.

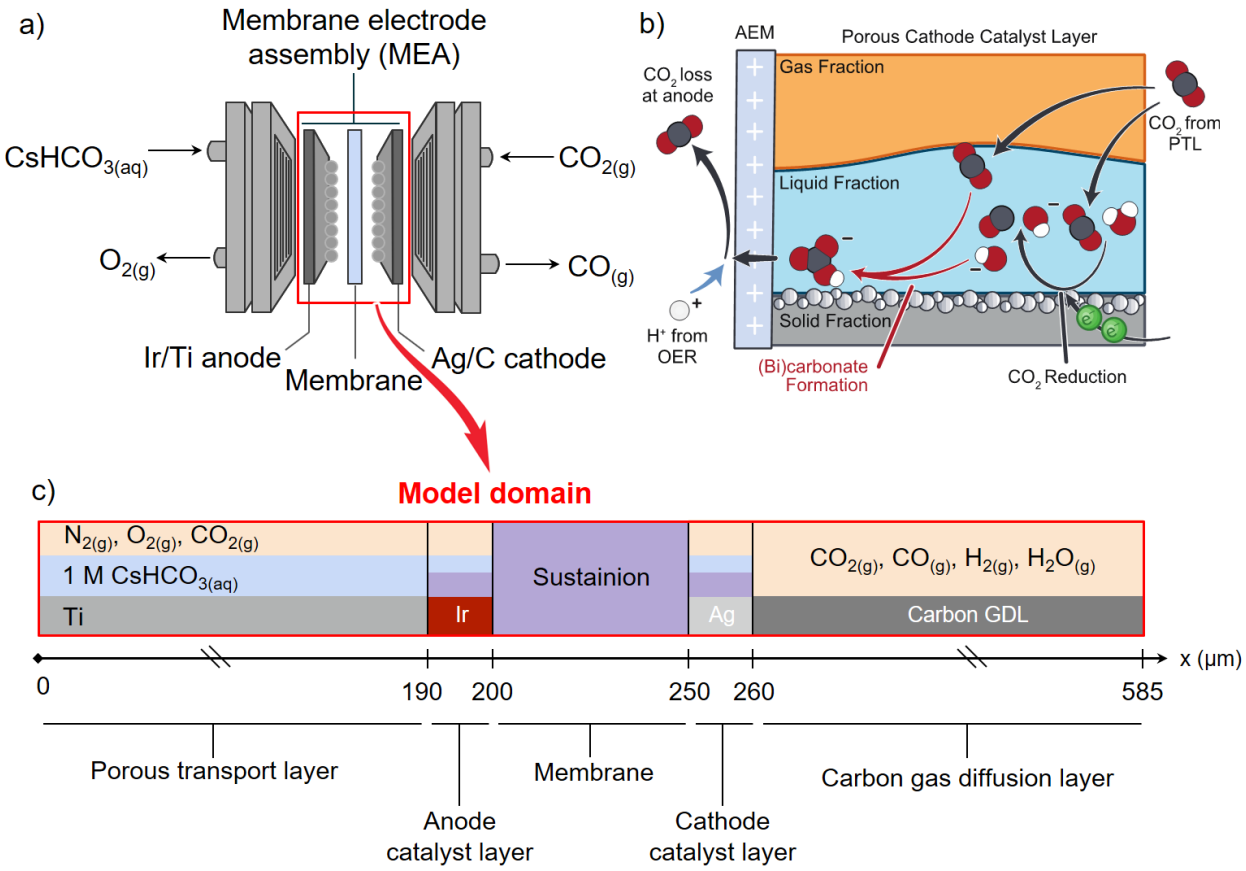

Figure 1: (a) Schematic diagram of a CO_2 reduction (CO2R) electrolyzer MEA with anodic and cathodic feedstocks of 1 M $CsHCO_3$ and humidified CO_2, respectively. (b) Schematic diagram showing the processes of CO_2 reduction, (bi)carbonate formation and crossover, and CO_2 loss at the anode. (c) 1-D continuum model domain showing the gas, liquid, solid, and ionomer phases.

Experimentally, the CO2R electrolyzer was operated at constant cell potentials ranging from 2.35 to 4.00 V while measuring the partial current densities for CO and H_2 formation (**Figure 2a, b**).[19] The CO formation rate increased to a peak value of 300 mA cm^{-2} as the potential was increased to 3.20 V. The CO partial current density then decreased as the potential was increased to 4.00 V, and the H_2 partial current density increased to 850 mA cm^{-2}. The model was fit to the

experimentally-measured polarization data by adjusting the parameters in the MHC expression for the rate of CO_2 reduction (*i.e.*, $k_{0,CO}$ and λ_{reorg}; Eq. (17)) and in the Tafel equation for HER (*i.e.*, $i_{0,HER,base}$ and $\alpha_{c,HER}$; Eq. (14)) while holding the other model parameters constant. Quantitative agreement between the model and experimental CO partial current densities is observed for the MHC model when λ_{reorg} = 1.35 eV is used (**Figure 2a**). This value agrees with the range of fitted values of λ_{reorg} (0.8 to 2.0 eV)[20] for CO2R experiments performed with planar silver cathodes (see **Supplementary Note 1** and **Figure S1** for sensitivity analysis and more details on the physical interpretation of this value). Moreover, the charge-transfer coefficient for H_2 ($\alpha_{c,HER}$ = 0.13) agrees well with a recent study using continuum modeling to resolve kinetic parameters of H_2 formation on planar silver[21]. The applied-voltage breakdown (**Figure S2**) demonstrates that the kinetic overpotentials are the dominant contributors to the overall cell voltage. The high overpotential associated with the CO evolution reaction (COER) highlights the need to develop more efficient electrocatalysts. Moreover, the ionic and electrical resistances account for >300 mV of voltage loss at 1000 mA cm^{-2}. This result indicates that more conductive porous-transport layers and membranes may also improve performance.

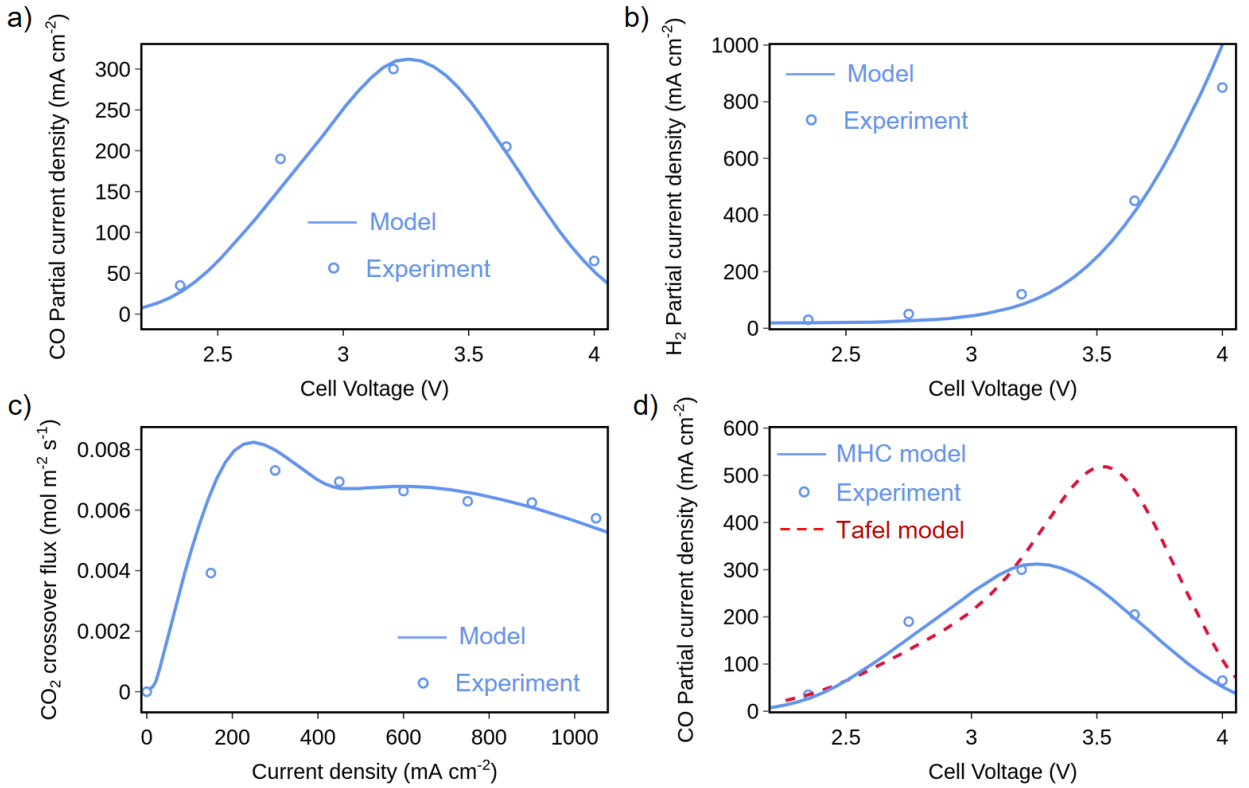

Figure 2: Experimental and modeled partial current densities for (a) CO and (b) H_2 formation as a function of cell voltage. (c) Experimental and modeled CO_2 crossover fluxes. (d) Comparison of experimental CO partial current densities with simulated results obtained with Marcus-Hush-Chidsey (MHC) and Tafel models.

To validate the mass-transport framework used in the model, the simulated and experimentally-measured CO_2 crossover fluxes were compared over a current density range of 0 to 1,050 mA cm^{-2} (**Figure 2c**). Good agreement is observed between the model and experiment at high current densities; however, the model slightly over predicts the CO_2 crossover flux at lower current densities. This discrepancy exists because CO_2 bubbles that form in the anode chamber are recirculated to the anolyte $CsHCO_3$ reservoir by the peristaltic pump. This process provides the opportunity for CO_2 to re-dissolve and buffer the anolyte, which decreases the amount of CO_2 in the anolyte headspace measured experimentally. A model that encompasses the along-the-channel effects and anolyte reservoir is necessary to capture this effect.

MHC theory has been employed widely in the field of electrochemical engineering because it accounts for electron-transfer limitations at high overpotentials and the free-energy change associated with reorganizing the solvent after electron transfer[22]. In contrast, the Tafel model (Eq. (19)) assumes ion-transfer limits the overall rate of CO2R[23]. These two models both exhibit good agreement between the experimental data at low cell potentials where electron-transfer limitations are not expected (**Figure 2d**). The agreement between the Tafel model and experiment at low potentials shows that the kinetic parameters obtained from experiments with planar silver electrodes are reasonably transferable to MEA experiments[21]. However, the Tafel model over predicts the CO formation rate at high cell potentials, even when mass-transport effects are taken into account. We considered that agreement between the experimental data and Tafel model could be improved by incorporating a fitted film resistance into the effective overpotential (Eq. (20); **Figure S3**). The film resistance improves agreement between the Tafel model and experimental CO partial current densities at high cell potentials at the expense of agreement at low cell potentials. However, the fitted film resistances (10^2 Ω cm^2) are larger than the values expected from measurements of silver oxide films[24]. Collectively, these results suggest that both electron-transfer and mass-transfer limitations occur for CO_2R in MEAs and that film resistances cannot explain curvature in the CO partial current density data. The need to use MHC to capture these electron-transfer limitations is consistent with the calculation of large barriers for solvent reorganization[23], although further experimental investigation is needed to confirm this.

Because CO_2 reduction involves bond breaking and re-forming, there must be a contribution associated with ion transfer in addition to electron transfer. This mechanistic

interpretation suggests the need for models beyond MHC, which purely accounts for electron transfer, towards models of coupled ion electron transfer (CIET) that account for barriers associated with ion transfer and electron transfer. Work by Bazant[23] has demonstrated that the rate law for an electron-transfer limited CIET is similar to the MHC kinetics utilized herein that provides the best fit to our experimental data (see **Supplementary Note 2**), where the contribution associated with ion transfer is found in the pre-factor of the rate expression. Accordingly, the value of $k_{0,CO}$ fit to the MHC kinetics used in the present study can be considered a lumped parameter that implicitly includes the effect of ion transfer on the rate of CO2R. This analysis suggests that CO2R is likely governed by coupled ion-electron transfer kinetics in the limit of electron transfer limited CIET. The use of electron-transfer limited CIET can also potentially explain the high value of the fitted reorganization energy, because this limit is most applicable when the effective ion transfer free energy barrier and the magnitude of the formal overpotential are much smaller than the reorganization energy.

The assertion that CO2R occurs *via* an electron-transfer limited CIET is further supported by alternatively considering CIET in the ion-transfer limit. Bazant's work on CIET also introduced a rate expression for ion-transfer limited CIET[23], which is similar to the BV kinetics (now with a pre-factor that accounts for barriers associated with electron transfer) that struggle to fit our experimental data. Hence, similar to how BV kinetics are shown to not be descriptive of our experimental data, ion-transfer limited CIET is also unlikely to explain polarization data observed in CO2R (see **Supplemental Note 3**), suggesting that electron-transfer limitations, rather than ion-transfer limitations, dictate observed rates.

2.2 Transport of CO_2 and ionic species

The validated model was used to investigate the transport of CO_2 and ionic species in the CO2R MEA (**Figure 3**). At 0 mA cm^{-2}, the pH throughout the MEA resembles that of the 1 M $CsHCO_3$ solution and the CO_2 concentration profile is indicative of the gradient between the bulk concentration of CO_2 present in the anode chamber and the maximum solubility of CO_2 in 1 M $CsHCO_3$ at 50°C for a gas phase containing 88 wt% CO_2 and 12 wt% H_2O (14.7 mM; **Figure 3a**). As the current density increases, the CO_2 concentration increases in the anode catalyst layer as H^+ produced by acidic OER decreases the local pH (**Figure 3b**), shifting the (bi)carbonate equilibrium towards HCO_3^- (**Figure 3c**).[25] Concurrently, the pH in the cathode catalyst layer increases to >14 at 1000 mA cm^{-2} due to hydroxide formation (**Figure S4a)**. This elevated current density decreases the CO_2 concentration at the cathode by consuming CO_2 to form CO, shifting the (bi)carbonate equilibrium from CO_2 to CO_3^{2-} (**Figure 3d**), and increasing the total ionic concentration of the solution, thereby reducing the CO_2 solubility. A main contributor to the reduced solubility of CO_2 is the high concentration of cesium cations present in the cathode at high current densities (**Figure S4b**), which originate from the anode and decrease the Henry's constant from 14.7 mM atm^{-1} CO_2 to 2 mM atm^{-1} CO_2 per Eq. (53). Consistent with previous studies, the Donnan exclusion effect of the AEM is not strong enough to block cation transport from anode to cathode[26]. The net result of these phenomena is a decrease in reactant CO_2 available for the CO2R, and consequently, a decrease in CO formation rates at high cell potentials (**Figure 2a**). Other possible effects of cesium on the rate of CO2R and HER are discussed in **Supplementary Note 4**.

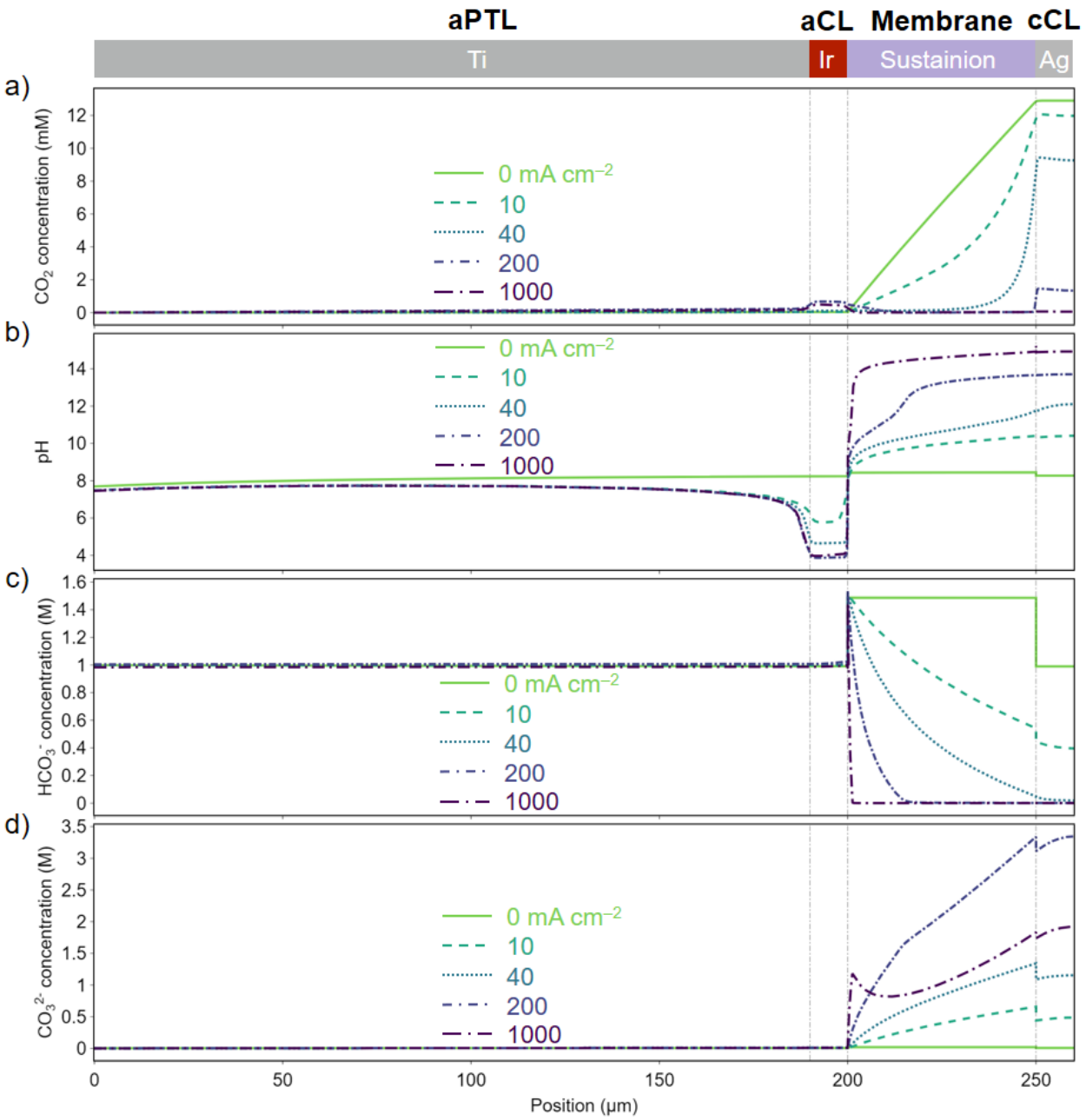

Figure 3: Modeled (a) CO_2 concentration, (b) pH, (c) HCO_3^- concentration, and (d) CO_3^{2-}as a function of current density and position in the membrane electrode assembly (MEA).

The partial pressure of CO in the cathode catalyst layer increases as the current density is increased from 0 to 200 mA cm^{-2} before decreasing at the onset of H_2 evolution (**Figure S5a, b**). The CO_2 partial pressure decreases because CO_2 dissolves and reacts in the cathode catalyst layer (**Figure S5c**). The H_2O partial pressure in the cathode catalyst layer decreases throughout the GDL

as the current density is increased from 200 to 1000 mA cm^{-2} due to the pressure drop and consumption of water by the CO2R and HER. In the anode, the partial pressure of CO_2 increases as the current density increases from 0 to 200 mA cm^{-2} due to a rise in CO_2 concentration in the electrolyte (**Figure S6a**). However, at 1000 mA cm^{-2}, the CO_2 partial pressure in the anode decreases because as the partial pressure of O_2 increases (**Figure S6b**) and the equilibrium between the CO_2 in the gas- and electrolyte-phases is established These non-intuitive results demonstrate the importance of modeling the dynamics of the gas-phase and the CO_2 phase equilibrium.

To understand the crossover of carbon from cathode to anode (**Figure 2c**), we examined the transference numbers in the MEA. The $CsHCO_3$ delivered to the anode generates a HCO_3^- concentration gradient that drives the transport of HCO_3^- from anode to cathode against the potential gradient. Consequently, a negative transference number for HCO_3^- is observed in the membrane at 10 mA cm^{-2} (**Figure 4a**). To maintain charge-conservation, CO_3^{2-} is transported from cathode to anode with a transference number of ~2 in the membrane at 10 mA cm^{-2} (**Figure 4b**). These opposing fluxes of carbon yield a proportional relationship between CO_2 crossover flux and current density from 0 to 200 mA cm^{-2}. The decrease and subsequent plateau in CO_2 crossover at 200 mA cm^{-2} coincide with the appearance of CO_3^{2-} as the sole charge-carrying species in the membrane. As the current density is increased to 1000 mA cm^{-2}, hydroxide emerges as the main charge carrier through the membrane (**Figure 4c**), which reduces Ohmic losses due to the faster diffusion of OH^- relative to CO_3^{2-}. This transition in charge-carrying species from CO_3^{2-} to OH^- also decreases the CO_2 crossover flux, however, CO_2 is still measured in the anode effluent of the

electrolyzer due to the continuous conversion of HCO_3^- from the anode feedstock into CO_2. Consequently, HCO_3^- remains the dominant charge-carrier in the anode at all current densities (**Figure 4a**). The abrupt changes in transference numbers seen in the membrane are a result of the pH gradient through the membrane, which transform HCO_3^- fed to the anode into CO_3^{2-} and CO_3^{2-} originating from the cathode into HCO_3^-. The flux of dissolved CO_2 accounts for less than 1% of the total dissolved carbon that crosses the membrane. The results here underscore the opportunity to operate at high current densities where OH^- is the charge-carrier to reduce Ohmic losses and the need to model both the anode and cathode of a CO_2 electrolyzer to describe electrolyzer performance accurately.

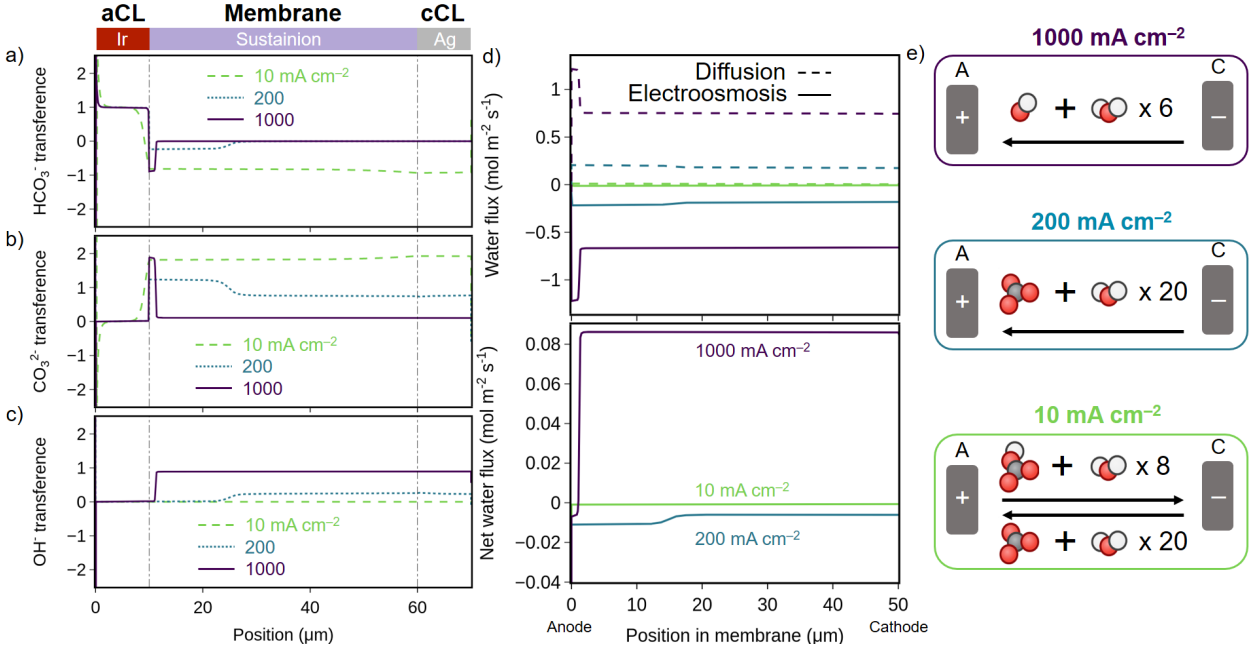

Figure 4: Modeled transference numbers for (a) HCO_3^- (b) CO_3^{2-} and (c) OH^- in the MEA as a function of current density. (d) Modeled water fluxes across the membrane due to diffusion (dashed lines) and electroosmosis (solid lines) and net water flux as a function of current density (e) Diagram showing the number of water molecules moved by electroosmosis between the anode and cathode depending on the dominant charge-carrying species.

2.3 Water transport and electroosmosis

Water transport in the membrane is driven by chemical potential and ionic gradients (*i.e.*, current), which lead to a decrease in water activity and liquid water pressure in the membrane as the current density is increased (**Figure S7**). The diffusional flux of water (from anode to cathode) is directly proportional to the water activity gradient in the MEA, whereas the flux of water due to electroosmosis is dependent on the ionic charge carrier because the electroosmotic coefficient is roughly equal to the number of water molecules in each ions hydration shell (Eq. (58) and (59))[27]. As shown in **Figure 4d**, the flux of water associated with diffusion and electroosmosis both increase with increasing current density. At 10 mA cm^{-2}, the diffusional flux of water is balanced by electroosmosis. The average electroosmotic coefficient in this current density regime is 12, because HCO_3^- and CO_3^{2-} move in opposite directions along with 8 and 20 water molecules, respectively (**Figure 4e**). At 200 mA cm^{-2}, the flux of HCO_3^- approaches 0 (**Figure 4a**), and therefore, the average electroosmotic coefficient corresponds to that of CO_3^{2-} (*i.e.*, $\zeta_{CO_3^{2-}} = 20$). The flux of water associated with electroosmosis at 200 mA cm^{-2} is higher than the flux of water due to diffusion as a result of the high electroosmotic coefficient of CO_3^{2-}, and therefore the net water flux is negative (from cathode to anode). At 1000 mA cm^{-2}, water transport by diffusion is greater than water transport by electroosmosis because OH^- (with an electroosmotic coefficient of $\zeta_{OH^-} = 6$) becomes the majority charge-carrier, giving rise to a positive net water flux. This interplay points to intermediate current densities (200 mA cm^{-2}) as being most susceptible to membrane dehydration due to the high electroosmotic coefficient of CO_3^{2-} relative to OH^-, which is a non-

intuitive result and arising from the complicated coupling of interspecies transport and reaction rates.

The net electroosmotic coefficient (denoted as β; Eq. (60)) describes how much water is transported through the membrane from anode to cathode relative to the amount of water consumed by the electrochemical reactions (**Figure S8**). At low current densities (*i.e.*, 10 mA cm^{-2}), β is negative, which means that the net flux of water is directed away from the cathode, indicating that water must come from the humidified CO_2 gas to supply the reactant for the CO2R and HER. As the current density is increased to the point at which CO formation rate is at its maximum (500 mA cm^{-2}), β becomes positive. At 1000 mA cm^{-2}, β increases to ~0.8. This result indicates that when OH^- is the dominant charge-carrier, enough water is transported through the membrane to sustain the electrochemical reactions. Accordingly, the use of a humidified CO_2 feed may not be necessary at high current densities when a liquid anolyte feed is used. These results show that water is not the limiting reagent in CO2R. Nonetheless, water management is still critical in CO2R electrolyzers because it impacts the Ohmic losses and transport of species in the membrane.

2.4 Effect of catalyst-layer thickness and surface area on CO2R and HER

The validated model allows for the investigation of key properties and virtual experiments to provide design guidance by analyzing the complex tradeoffs endemic to this system. Herein, the cathode catalyst-layer thickness and specific surface area (SSA) were explored. The model demonstrates that reducing the cathode catalyst-layer thickness from 10 to 1 μm decreases the partial current density for CO (**Figure 5a**) and H_2 formation (**Figure S9a**). The

H_2 partial current density decreases more than the CO partial current density, which leads to a lower faradaic efficiency for CO (FE_{CO}) at high current densities (**Figure S9b**). The lower H_2 partial current density with thinner catalyst layers comes as a result of the lower surface area relative to the thicker catalyst layers. Moreover, at a constant current density, the pH is higher in the smaller volume of the thinner catalyst layers for the same flux of OH^- from the CO2R and HER (**Figure S9c**). The higher pH in the thinner catalyst layer reduces the CO_2 concentration (**Figure S9d**). The CO partial current density is therefore more sensitive to increasing the catalyst-layer thickness than the partial current density for the HER because of the compounding effects of increased surface area and CO_2 reactant concentration. While these phenomena lead to a higher CO partial current density with thicker catalyst layers, the CO_2 utilization (*i.e.*, the amount of CO formed divided by the amount of CO_2 that is reacted to form HCO_3^- and CO_3^{2-} and subsequently released at the anode; Eq. (85)) follows the opposite trend (**Figure 5b**). This tradeoff suggests an optimum catalyst layer thickness of 5 μm to simultaneously enable a CO partial current density > 200 mA cm^{-2} and CO_2 utilization efficiency > 60 %.

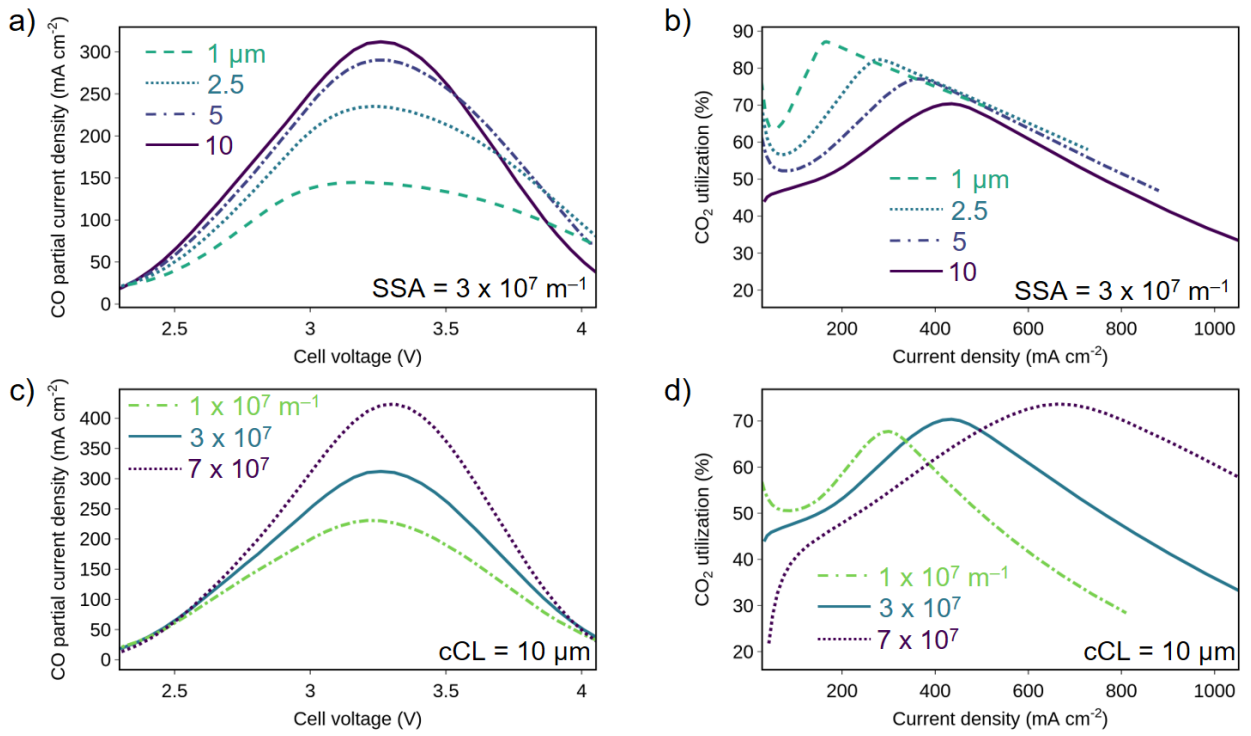

Figure 5: Partial current density for (a) CO formation as a function of cell voltage and (b) CO_2 utilization as a function of total current density for cathode catalyst layers with thicknesses of 10, 5, 2.5, and 1 μm at a constant specific surface area (SSA) of 3 x 10^7 m^{-1}. (c) Partial current density for CO formation as a function of cell voltage and (d) CO_2 utilization as a function of total current density for catalyst layers with a SSA of 1 x 10^7, 3 x 10^7, and 7 x 10^7 m^{-1} at a constant cathode catalyst-layer thickness of 10 μm. The basecase simulation results are shown with solid lines.

Catalyst specific surface area (SSA) is another important characteristic of CO2R electrolyzers that is inversely proportional to the size of the catalyst particles as per Eq. (22). The model shows that increasing the SSA (*i.e.*, reducing the particle size while maintaining the catalyst mass) increases both the CO partial current density (**Figure 5c**) and H_2 partial current density (**Figure S10a**) due to a higher availability of surface sites for electron-transfer. The lower SSA catalyst layers achieve a higher peak FE_{CO} (**Figure S10b**) due to the lower onset potential for H_2 formation, but this peak diminishes at the onset of CO evolution. The higher CO partial current density with higher SSA catalyst layers is enabled by a higher surface area for transport of CO_2 across the gas/ionomer interface, as per Eq. (52). The faster transport of CO_2 across the ionomer

layer yields a higher CO_2 concentration relative to the maximum solubility (**Figure S10c**). Consequently, the increased CO formation rates enabled by decreasing particle size come at the expense of increased crossover of CO_2 across the membrane (**Figure S10d**). At high current densities, however, the crossover of CO_2 is not strongly affected by catalyst particle size. Therefore, a higher CO_2 utilization is observed with smaller catalyst particles (**Figure 5d**). The implication of these results is that smaller catalyst particles enable higher CO formation rates than larger catalyst particles without increasing the rate of HER or decreasing the CO_2 utilization at high current densities.

The thickness of the GDL was found to have a less significant impact on CO formation in MEAs than catalyst layer thickness and specific surface area (**Figure S11**). Decreasing the GDL thickness from the nominal value for Sigracet 39BC (325 μm) to 100 μm led to a smaller gas-phase pressure drop between the flow channel and cathode catalyst layer. Consequently, a higher partial pressure for CO_2 is observed in the cathode catalyst layer for thinner GDLs (**Figure S11a**), which increases the concentration of CO_2 in the electrolyte. This higher CO_2 concentration modestly increases the peak CO partial current density (**Figure S11b**).

2.5 Effect of anolyte pH and membrane IEC on CO2R and HER

HCO_3^- is commonly used as a buffering anion for CO2R because it lowers the pH rise at the cathode to reduce the rate of conversion of CO_2 to (bi)carbonates[28, 29]. However, Sustainion is much more conductive in its OH^- form than in its HCO_3^- form[7]. To examine these tradeoffs, we simulated a CsOH anolyte and compared the results to those obtained with $CsHCO_3$. Switching

the anolyte from $CsHCO_3$ to CsOH increases the average conductivity of the membrane from ~12 mS cm^{-1} to ~25 mS cm^{-1} (**Figure S11a**), which reduces the Ohmic resistance associated with ion transport. These results are consistent with independent conductivity measurements documented in a previous study[30]. Accordingly, the cell voltage for maximum CO formation is shifted to 3 V with CsOH, compared to 3.3 V with $CsHCO_3$ (**Figure S12b, c**). The lower peak in the CO formation rate with CsOH compared to $CsHCO_3$ is caused by the higher pH in the cathode catalyst layer (**Figure S12d**). This higher pH with CsOH decreases the CO formation rate by decreasing the concentration of CO_2 in the cathode relative to $CsHCO_3$ (**Figure S13a**). Additionally, the CsOH anolyte increases the net electroosmotic coefficient relative to $CsHCO_3$ (**Figure S13b**) because of the larger flux of OH^- relative to HCO_3^- and CO_3^{2-}, which increases the water activity at the cathode, thereby giving rise to faster HER kinetics.

The conductivity of the membrane is directly correlated with the concentration of fixed-charge groups (*i.e.*, the ion exchange capacity; IEC). Although commonly used, Sustainion has a notably low IEC compared to other AEMs[14]. The model shows that increasing the IEC of the membrane from 1.2 to 2.0 mmol g^{-1} leads to a dramatic increase in the CO partial current density (**Figure 6a**). In contrast, the H_2 partial current density is not strongly impacted by an increase in IEC (**Figure S14a**). The higher IEC membranes expectedly exhibit higher conductivities (**Figure 6b**). However, the high IEC membranes also decrease the pH (**Figure 6c**) in the cathode catalyst layer by excluding co-ions (*e.g.*, H^+, K^+) *via* Donnan exclusion, trapping them in the cathode catalyst layer, while also more efficiently transporting alkaline, counter-ion species (*i.e.*, CO_3^{2-} and OH^-) away from the cathode catalyst layer, which reduces the overpotential that drives HER. The

lower HER overpotential has a larger impact on the H_2 partial current density than the increased conductivity, therefore, a slightly lower H_2 partial current density is observed for membranes with a higher IEC (**Figure S14a**). It is important to note that the model does not account for the effect of IEC on the swelling behavior and mechanical integrity of the ionomer, which could lead to a decrease in CO partial current density performance as the IEC is increased.

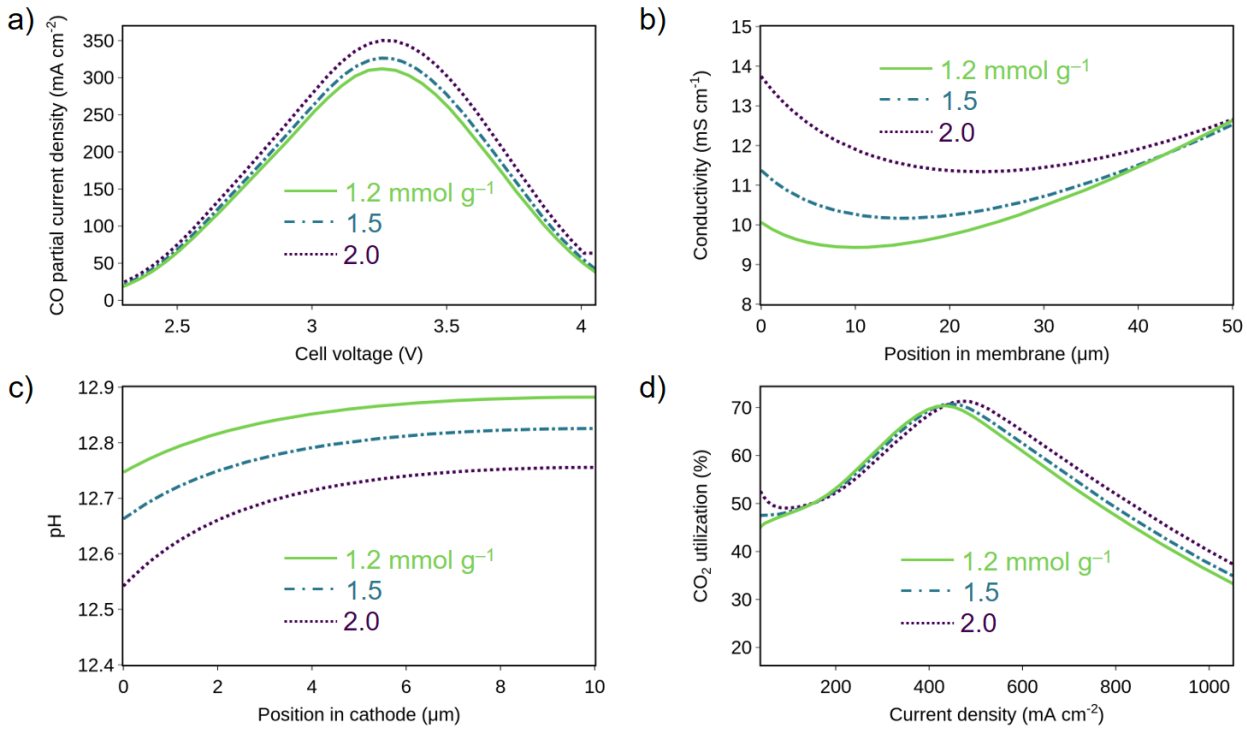

Figure 6: (a) CO and (b) H_2 partial current density as a function of cell voltage for simulated ion exchange capacities (IECs) of 1.2, 1.5, and 2.0 mmol g^{-1}.(c) ionic conductivity of the different IEC membranes at a cell potential of –2.3 V. (d) pH in the cathode catalyst of the different IEC membranes at a constant total current density of 100 mA cm^{-2}. The basecase simulation results are shown with solid lines.

The lower pH in the cathode catalyst layer observed in the higher IEC membranes reduces the extent of CO_2 conversion into CO_3^{2-}, thereby enabling a higher CO_2 concentration (**Figure**

S14b). This effect, combined with the higher conductivity of the higher IEC membranes, explains why a higher CO partial current density is observed. The higher IEC membranes also increase the crossover of carbon from cathode to anode because of the higher affinity for CO_3^{2-} transport over OH^- transport (**Figure S15**). However, the increase in CO formation rate enabled by higher IEC membranes is larger than the increase in CO_2 crossover rate, which results in higher CO_2 utilization (**Figure 6d**). Collectively, these results show that increasing the IEC of the membrane provides a means for increasing CO formation rates without enhancing the rate of the HER or reducing CO_2 utilization.

Hydroxides can neutralize the positively-charged imidazolium groups in ionomer membranes, leading to "current induced membrane discharge" (CIMD)[31]. Our simulation shows that CIMD decreases the CO partial current density at all potentials relative to the basecase, which assumes a unity fraction of protonated imidazolium groups (*i.e.*, no CIMD occurs; **Figure S16a**). The decrease in CO formation caused by CIMD is more pronounced for more weakly basic fixed-charge sites (*i.e.*, sites with higher pK_b values; see **Supplementary Note 5**). For a pK_b of –2, the simulation results are nearly identical to the basecase. The CO_2 crossover flux is shown to decrease with increasing pK_b values due to a lower uptake of HCO_3^- and CO_3^{2-} in the membrane (**Figure S16b**). This phenomenon occurs because of the reduced fraction of protonated imidazolium groups in the membrane (**Figure S16c**). The reduced concentration of protonated imidazolium increases the concentration of Cs^+ in the membrane, thereby increasing the propensity for precipitation in CO_2 electrolyzers (**Figure S16d**). These results indicate that increasing AEMs must furnish highly concentrated and basic fixed-charge groups to enable high CO formation rates.

3. Conclusions

In this study, we used a 1-D continuum model validated against measured experimental data to investigate the myriad of coupled phenomena occurring in membrane-electrode assemblies (MEAs) undergoing CO_2 reduction. The model reveals that both mass- and electron-transfer limitations dictate limiting current densities for CO2R. The latter effect necessitates use of MHC theory to reproduce experimental behavior and highlights the need for further studies investigating the nature of electron transfer and solvent reorganization in CO2R. This study demonstrates how continuum modeling can be used to link quantum mechanical theories of electron transfer with device-scale performance.

The simulations show that CO_2 and water transport across the MEA is defined by the principal charge-carrying species in the membrane, which varies depending on the current-density regime. At low current densities (40 mA cm^{-2}), the transport of HCO_3^- from anode to cathode against the potential gradient decreases the amount of CO_2 emitted at the anode and reduces the net flux of water from anode to cathode. At intermediate current densities (200 to 1000 mA cm^{-2}), CO_3^{2-} is the sole charge-carrier, which increases the flux of CO_2 and water from cathode to anode, thereby reducing the concentration and activity of water and CO_2 at the cathode, respectively. Finally, at high current densities (1000 mA cm^{-2}), the high pH in the MEA gives rise to OH^- as the principal charge carrying species. The transport of OH^- reduces the crossover of carbon and water from cathode to anode, which leads to improved hydration and conductivity of the membrane.

Model sensitivity analyses performed on the anolyte, catalyst layer, and membrane properties demonstrate the trade-off between CO formation rates and carbon crossover in CO2R electrolyzers that arise due to coupling between interspecies ionic and water transport and various chemical and electrochemical kinetics. Thicker catalyst layers yield higher CO formation rates, but also lower CO_2 utilizations. Catalyst layers with higher SSAs (*i.e.*, catalysts with smaller particle sizes) increase the CO formation rate without negatively impacting CO_2 utilization at high current densities. Membranes with higher IEC reduce Ohmic resistances and lower the pH at the cathode, which benefits CO formation and increases CO_2 utilization without enhancing deleterious HER. Collectively, these results provide insights into the dynamics of water and ion transport in CO2R electrolyzers and present different materials optimization strategies that inform future experiments. Furthermore, this study highlights the importance of using self-consistent (electro)chemical-engineering fundamentals to explore and unravel such complex systems.

4. Methods

4.1 Governing equations for charge, mass, and momentum transport

Electron transport in the conductive solid-phases (Ti anode transport layer, Ir-oxide anode catalyst layer, Ag cathode catalyst layer, and carbon gas-diffusion layer) was modeled using Ohm's law,

$$\boldsymbol{\nabla} \cdot \mathbf{i}_s = -\boldsymbol{\nabla} \cdot (\sigma_{\text{eff}} \phi_s) \tag{1}$$

where $\boldsymbol{i_s}$ and ϕ_s represent the current density and electric potential in the solid electron-conducting phases. The effective conductivity (σ_{eff}) of the porous electron-conducting phases was determined using a Bruggeman relation,

$$\sigma_{\text{eff}} = {\varepsilon_S}^{1.5}\sigma_s \tag{2}$$

where ε_S and σ_s are the volume fraction and nominal conductivity of the solid conductor, respectively (see **Table S1** for values). The governing equations for mass transfer of each chemical species j in the gas-phase (j = $CO_{2(g)}$, $CO_{(g)}$, $H_{2(g)}$, and $H_2O_{(g)}$) and i in the electrolyte-phase (i = $H^+_{(aq)}$, $OH^-_{(aq)}$, $HCO_3^-{}_{(aq)}$, $CO_3^{2-}{}_{(aq)}$, $CO_{2(aq)}$, and $Cs^+_{(aq)}$) are,

$$\boldsymbol{\nabla} \cdot \boldsymbol{J_j} = \varepsilon_G \sum_j M_j R_{k,j} \tag{3}$$

$$\boldsymbol{\nabla} \cdot \boldsymbol{n_i} = (\varepsilon_L + \varepsilon_I) \sum_i R_{k,i} \tag{4}$$

where $\boldsymbol{J}_j$ and M_j are the mass flux and molecular weight of gaseous species j, respectively, ρ_G is the density of the gas-phase, $\boldsymbol{u_G}$ is the mass-averaged velocity of the gas-phase, $\boldsymbol{n_i}$ is the molar fluxes of dissolved species i, ε_G is the gas-volume fraction, and $R_{k,i/j}$ is the volumetric rate of mole generation/consumption by process k of species i or j. The volume fraction of ionomer (ε_I) in the catalyst layers was determined based on the ionomer-to-catalyst mass ratio of 3 used in the precursor catalyst ink. The volume fractions of gas and liquid (ε_L) in the remainder of the void space were determined based on the capillary pressure (p_{cap}) in the catalyst layer using experimental water saturation data for Pt/C from Zenyuk *et al.*[32] (**Figure S16**) which was assumed to hold for Ag/C, where

$$p_{cap} = p_L - p_G \tag{5}$$

The implicit assumption of Eq. (4) is that the buffer reaction kinetics are the same in the ionomer and bulk electrolyte. While these kinetics may in fact vary between the two phases, previous work has shown that the kinetic parameters obtained from bulk electrolyte measurements provide accurate approximations of the (bi)carbonate buffer dynamics in AEMs[33].

The momentum balances on the liquid and gas phases are given as,

$$\boldsymbol{\nabla} \cdot (\rho_G \boldsymbol{u_G}) = Q_G \tag{6}$$

$$\boldsymbol{\nabla} \cdot (\rho_G \boldsymbol{u}_L) = Q_L \tag{7}$$

Where Q_G is the net rate of mass generation in the gas-phase. ρ_L, $\boldsymbol{u}_L$, and Q_L are the density, mass-averaged velocity, and net rate of mass generation in the liquid-phase.

4.2 Reaction chemistry

At the anode, iridium oxide catalyzes the oxygen-evolution reaction (OER) under acid and basic conditions,

$$2H_2O \rightarrow 4e^- + O_2 + 4H^+ \tag{8}$$

$$U^0_{\mathrm{OER}} = 1.23\ \mathrm{V\ vs.\ SHE, pH} = 0$$

$$4OH^- \rightarrow 4e^- + O_2 + 2H_2O \tag{9}$$

The silver cathode catalyst catalyzes the CO evolution reaction (COER) and the hydrogen-evolution reaction (HER), which occurs through both H^+ and H_2O reduction,

$$CO_2 + H_2O + 2e^- \rightarrow CO + 2OH^- \qquad U^0_{COER} = -0.11 \text{ V vs. SHE, pH} = 0 \tag{10}$$

$$2H_2O + 2e^- \rightarrow H_2 + 2OH^- \qquad U^0_{HER} = 0.0 \text{ V vs. SHE, pH} = 0$$

$$2H^+ + 2e^- \rightarrow H_2 \tag{11}$$

The electrochemical formation of H_2 through water and proton reduction is described by the following concentration-dependent Tafel expressions,

$$i_{HER,base} = -i_{0,HER,base} a_w exp\left(-\frac{\alpha_{c,HER} F}{RT}\eta_{HER}\right) \tag{12}$$

$$i_{HER,acid} = -i_{0,HER,acid}\left(\frac{c_{H^+}}{1\ M}\right) exp\left(-\frac{\alpha_{c,HER} F}{RT}\eta_{HER}\right) \tag{13}$$

Where $i_{0,HER,base}$ and $i_{0,HER,acid}$ are the exchange current densities for the HER in base and acid, respectively. $\alpha_{c,HER}$ and η_{HER} are the cathodic transfer coefficient and overpotential of HER, respectively. F is Faraday's constant (96485 C mol^{-1}), R is the ideal gas constant (8.314 J mol^{-1} K^{-1}), T is the temperature (323 K). These reactions were assumed to exhibit a first-order dependence on the reactant concentration (c_{H^+}) or water activity (a_w). Non-idealities were not considered for the ionic species (*i.e.,* H^+) due to the increased computational complexity and lack of available parameters for activity correlations for concentrated multi-component electrolytes. Therefore, the fitted exchange current densities employed in the model can be considered lumped parameters that encompass the non-idealities. The overpotential of each electrochemical reaction k (η_k)was calculated according to the reduction potential of reaction k at standard conditions (U^0_k), accounting for changes in the local pH using the Nernst equation,

$$\eta_k = \phi_s - \phi_i - \left(U_k^0 - \frac{2.303RT}{F}\mathrm{pH}\right) \tag{14}$$

The partial current densities for OER in acid ($i_{\mathrm{OER,acid}}$) and base ($i_{\mathrm{OER,base}}$) were modeled using concentration-dependent Tafel expressions similar to those used for the HER at the cathode[34],

$$i_{\mathrm{OER,acid}} = i_{0,\mathrm{OER,acid}} {a_w}^{1.6} \exp\left(\frac{\alpha_{a,\mathrm{OER}} F}{RT}\eta_{\mathrm{OER}}\right) \tag{15}$$

$$i_{\mathrm{OER,base}} = i_{0,\mathrm{OER,base}} \left(\frac{c_{\mathrm{OH^-}}}{1\ M}\right) \exp\left(\frac{\alpha_{a,\mathrm{OER}} F}{RT}\eta_{\mathrm{OER}}\right) \tag{16}$$

Where $i_{0,\mathrm{OER,base}}$ and $i_{0,\mathrm{OER,acid}}$ are the exchange current densities for the OER in base and acid, respectively. $\alpha_{a,\mathrm{OER}}$ and η_{OER} are the anodic transfer coefficient and overpotential of OER, respectively.

While HER and OER have been shown to follow a simple Tafel relationship[35], recent work has pointed to the need to account for the reorganization energy (λ_{reorg}) of the products, reactants, and solvent when modeling the CO2R reaction due to observed limitations in current density that cannot be solely attributed to mass transfer[20]. Therefore, a simplified asymptotic approximation of the indefinite integral in MHC theory is used to relate the partial current density of inner-sphere electron transfer to the overpotential and change in free energy of the solvent, products, and reactants in the absence of electron transfer[36, 37],

$$i_{\mathrm{COER}} = -k_{0,\mathrm{CO}} \left(\frac{c_{\mathrm{CO_2}}}{1\ M}\right)^{1.5} a_w \frac{\sqrt{\pi\lambda_{reorg}}}{1+\exp(\tilde{\eta}_{COER})} \mathrm{erfc}\left(\frac{\lambda_{reorg} - \sqrt{1+\sqrt{\lambda_{reorg}} + \tilde{\eta}_{COER}{}^2}}{2\sqrt{\lambda_{reorg}}}\right) \tag{17}$$

where $k_{0,CO}$ is a constant pre-exponential factor that relates to the attempt frequency for CO2R and erfc is the complementary error function. The rate order of 1.5 for CO formation with respect to CO_2 concentration was deduced based on experiments performed at different partial pressures of CO_2[38]. In MHC, λ_{reorg} is the energy barrier associated with the reorganization of the water network in the catalytic reaction environment to accommodate the quantum tunneling of electrons from the electrode to CO_2 (see **Figure S17** for a schematic depiction of solvent reorganization). $\tilde{\eta}_{CO}$ is the dimensionless overpotential which is defined as

$$\tilde{\eta}_{CO} = \eta_{\mathrm{CO}}\left(\frac{n_{\mathrm{CO}}F}{RT}\right) \tag{18}$$

For the sake of comparison with the MHC kinetics above, CO2R was also modeled using Tafel kinetics:

$$i_{\mathrm{COER}} = -i_{0,\mathrm{COER}}\left(\frac{c_{\mathrm{CO_2}}}{1\ M}\right)^{1.5} a_w \exp\left(-\frac{\alpha_{c,\mathrm{COER}}F}{RT}\eta_{\mathrm{COER}}\right) \tag{19}$$

Where $i_{0,\mathrm{COER}}$, $\alpha_{c,\mathrm{COER}}$, and η_{COER} are the exchange current density, cathodic transfer coefficient, and overpotential for the CO evolution reaction, respectively. Kinetic parameters are given in **Tables S2** and **S3**. There is precedent to account for a film resistance (R_{film}) within the overpotential term of Tafel expressions. This empirical kinetic formulation was also considered,

$$i_{\mathrm{COER}} = -i_{0,\mathrm{COER}}\left(\frac{c_{\mathrm{CO_2}}}{1\ M}\right)^{1.5} a_w \exp\left(-\frac{\alpha_{c,\mathrm{COER}}F}{RT}(\eta_{\mathrm{COER}} + i_{total}R_{film})\right) \tag{20}$$

The molar consumption of reactants and generation of products in the electrolyte by the charge-transfer (CT) reactions follows Faraday's Law,

$$R_{CT,\mathrm{i}} = \frac{a_v s_{i,k} |i_k|}{n_k F} \tag{21}$$

where n_k is the number of electrons transferred in the reaction, and $s_{i,k}$ is the stoichiometric coefficient for species i in reaction k (i.e., the OER, HER, or CO2R reaction). This source term applies to the generation and consumption of H^+, H_2O, OH^-, and CO_2. The catalyst-layer specific surface area (a_v) was determined using the geometric relationship from Weng *et al.*[17],

$$a_v = \frac{3\varepsilon_s}{r_p} \tag{22}$$

Where r_p is the average radii of the catalyst particles, which was estimated as 25 nm for the basecase simulation based on transmission-electron-microscopy (TEM) images (**Figure S18**).

Within the electrolyte-phase, the following homogeneous reactions between CO_2, OH^-, CO_3^{2-}, HCO_3^-, and H^+ occur,

$$\mathrm{H_2O} \overset{k_1, k_{-1}}{\leftrightarrow} \mathrm{H^+ + OH^-} \qquad K_1 = 1 \times 10^{-14}\ \mathrm{M^2} \tag{23}$$

$$\mathrm{CO_{2(aq)} + H_2O_{(l)}} \overset{k_2, k_{-2}}{\leftrightarrow} \mathrm{H^+_{(aq)} + HCO^-_{3(aq)}} \qquad K_2 = 4.27 \times 10^{-7}\ \mathrm{M} \tag{24}$$

$$\mathrm{HCO_3^-} \overset{k_3, k_{-3}}{\leftrightarrow} \mathrm{H^+ + CO_3^{2-}} \qquad K_3 = 4.58 \times 10^{-11}\ \mathrm{M^{-1}} \tag{25}$$

$$\mathrm{CO_{2(aq)} + OH^-} \overset{k_4, k_{-4}}{\leftrightarrow} \leftrightarrow \mathrm{HCO_3^-} \qquad K_4 = 4.27 \times 10^{7}\ \mathrm{M^{-1}} \tag{26}$$

$$\mathrm{HCO_3^- + OH^-} \overset{k_5, k_{-5}}{\leftrightarrow} \mathrm{H_2O + CO_3^{2-}} \qquad K_5 = 4.58 \times 10^{3}\ \mathrm{M^{-1}} \tag{27}$$

The consumption and generation of chemical species i (including water) by these buffer (B) reactions is governed by the law of mass action,

$$R_{B,i} = \sum_i s_{i,n}\left(k_n \prod_{s_{i,n}<0} {c_i}^{-s_{i,n}} - \frac{k_n}{K_n} \prod_{s_{i,n}>0} {c_i}^{s_{i,n}}\right) \tag{28}$$

where K_n is the equilibrium constant of buffer reaction n, $s_{i,n}$ is the stoichiometric coefficient of species i the corresponding bulk reaction n ($s_{i,n} < 0$ for reactants and $s_{i,n} > 0$ for products). k_n and k_{-n} are the forward and reverse reaction rate constants for reaction n, respectively. Parameters for these reactions are given in **Table S4**.

4.3 Ion transport

The molar ionic fluxes in the electrolyte ($\boldsymbol{n_i}$) were taken to occur via diffusion, migration, and convection under conditions where dilute-solution theory applies,

$$\boldsymbol{n_i} = -D_i^{\text{eff}}\left(\boldsymbol{\nabla} c_i + z_i \frac{F}{RT} c_i \boldsymbol{\nabla}\phi_I\right) + c_i \boldsymbol{u_L} \tag{29}$$

Here z_i is the charge of the mobile ionic species and ϕ_I is the ionic potential. Electroneutrality was assumed with consideration of the fixed-charges present in the catalyst-layer ionomers and membrane,

$$\sum_i z_i c_i + \varepsilon_I \rho_{\text{ionomer}} \text{IEC}_{\text{ionomer,effective}} = 0 \tag{30}$$

Where $\rho_{ionomer}$ and $\text{IEC}_{\text{ionomer,effective}}$ are the density and effective ion-exchange capacity (mol g^{-1} wet polymer) of the ionomer. The chemical equilibrium between the imidazolium groups in the Sustainion ionomer and hydroxides is,

$$c_{-NH_2} \rightleftharpoons c_{-NH_3^+} + c_{OH^-} \tag{31}$$

Where $-NH_2$ and $-NH_3^+$ are the deprotonated and protonated imidazolium groups. This equilibrium reaction results in neutralization of fixed-charge groups in the ionomer, (*i.e.,* current-induced membrane discharge) that reduces the effective ion-exchange capacity of the ionomer[31]. The isotherm describing this phenomena is given defined by the pK_B of the imidazolium groups ($pK_{B,ionomer}$),

$$\alpha_{CIMD} = \frac{c_{-NH_3^+}}{c_{-NH_3^+} + c_{-NH_2}} = \frac{1}{1 + \frac{c_{OH^-}}{10^{-pK_{B,\text{ionomer}}}}} \tag{32}$$

Where α_{CIMD} is the fraction of protonated imidazolium groups. The effective ion-exchange capacity of the ionomer is therefore given as,

$$\text{IEC}_{\text{ionomer,effective}} = \text{IEC}_{\text{ionomer}} \alpha_{CIMD} \tag{33}$$

The basecase simulation assumes $\alpha_{CIMD} = 1$ and the $pK_{B,ionomer}$ was varied for sensitivity analysis.

Within the catalyst layers, ion transport was assumed to occur through both liquid electrolyte and ionomer. To model this situation, we assumed a single electrolyte-phase composed of a mixture of electrolyte and ionomer with a density of fixed charges equal to the volume fraction of ionomer in the catalyst layer multiplied by the nominal fixed charge density of the ionomer. Physically, this formulation implies that that the fixed-charges present in the

ionomer are homogeneously dispersed in the electrolyte volume of the catalyst layer. The effective diffusion coefficients were determined based on the water mole fraction (x_i) and volume fraction of water in the ionomer Φ_{w},

$$D_i^{\mathrm{eff}} = {\Phi_{\mathrm{w}}}^q \frac{D_{i,w}}{x_w(1+\psi_{\mathrm{i}})} \tag{34}$$

where $D_{i,w}$ is the diffusion coefficient of species i in water (**Table S5**), q is a tortuosity parameter that was fit to experimentally-measured conductivity data of Sustainion measured in bicarbonate and hydroxide forms[7], ψ_{i} is the ratio between species-solvent and species-membrane interaction effects, which depend on the reduced molecular weight of species i in the membrane ($M_{\mathrm{i,M}}$) and in water ($M_{\mathrm{i,w}}$),

$$\psi_{\mathrm{i}} = \frac{1}{\lambda}\left(\frac{V_{\mathrm{M}}}{V_{\mathrm{w}}}\right)^{\frac{2}{3}}\left(\frac{M_{\mathrm{i,M}}}{M_{\mathrm{i,w}}}\right)^{\frac{1}{2}} \tag{35}$$

$$M_{i,M} = \left(\frac{1}{M_i} + \frac{1}{M_M}\right)^{-1} \tag{36}$$

$$M_{i,w} = \left(\frac{1}{M_i} + \frac{1}{M_w}\right)^{-1} \tag{37}$$

where M_M is the molecular weight of the membrane, which is set to an arbitrarily large value of 10,000 g mol^{-1} and V_{w} is the molar volume of water. The molar volume of the membrane (V_M) was calculated based on the ion-exchange capacity and the dry density of the ionomer,

$$V_M = \frac{1}{\rho_{ionomer} IEC} \tag{38}$$

The mole fraction (x_w) and volume fraction of water (Φ_w) in the ionomer were calculated using the water uptake (λ) assuming free swelling,

$$x_w = \frac{\lambda}{1+\lambda} \tag{39}$$

$$\Phi_w = \frac{\lambda V_w}{\lambda V_w + V_M} \tag{40}$$

The λ value was determined as a function of water activity and the fraction of imidizolium groups exchanged with carbonates or hydroxides based on constant temperature water-uptake measurements for Sustainion (**Figure S19**)[39]. While the co-ion (Cs^+) is known to also impact the water uptake, this data is not available in the literature and therefore is neglected in the model. Donnan equilibrium was imposed at each interface to maintain charge-neutrality in the catalyst and membrane layers,

$$\phi_{i,x^+} - \phi_{i,x^-} = -\frac{RT}{z_i}\ln\left(\frac{c_{i,x^+}}{c_{i,x^-}}\right) \tag{41}$$

Where ϕ_{i,x^+} is the electrolyte potential on the right-side of the interface and ϕ_{i,x^-} represents the same quantity on the left-side of the interface. Similarly, c_{i,x^+} and c_{i,x^-} are the concentrations on the right and left side, respectively. The convective velocity of the liquid-phase ($\boldsymbol{u_L}$) in the CL pores was determined using Darcy's law,

$$\boldsymbol{u_L} = -\frac{\kappa^0_{sat}\kappa_{rL}}{\mu_L}\frac{(1-\varepsilon_S)^3}{(\varepsilon_S)^2}\boldsymbol{\nabla} p_L \tag{42}$$

where μ_L is the liquid viscosity, p_L is the pressure of the liquid-phase, and κ_{sat}^0 is the bulk saturated permeability (**Table S1**). The relative permeability (κ_{rL}) of the liquid-phase was estimated based a cubic dependency on water saturation,

$$\kappa_{rL} = \mathrm{S}^3 \tag{43}$$

4.4 Gas transport

The mass flux of each gas-phase species ($\boldsymbol{J}_j$) was calculated using Stefan-Maxwell equations for multi-component mass transport with consideration of convection,

$$\boldsymbol{J_j} = -\rho_g D_j^{\mathrm{eff}} \boldsymbol{\nabla}\omega_j - \rho_G D_j^{\mathrm{eff}} \omega_j \frac{\boldsymbol{\nabla} M_n}{M_n} + \rho_j \boldsymbol{u_G} \tag{44}$$

where ω_j is the mass fraction of gas species j, ρ_j is the mass concentration of gas species j, and M_n is the average molecular weight. The effective diffusion coefficients (D_j^{eff}) were calculated based on the molecular diffusion coefficients (D_j^m) and Knudsen diffusion coefficients (D_j^k) while accounting for the porosity of a porous medium using the Bruggeman correlation,

$$D_j^{\mathrm{eff}} = \varepsilon_G^{1.5} \left(\frac{1}{D_j^m} + \frac{1}{D_j^k} \right)^{-1} \tag{45}$$

$$D_j^k = \frac{2r_{\mathrm{p}}}{3} \sqrt{\frac{8RT}{\pi M_i}} \tag{46}$$

The molecular diffusion coefficients were determined based on the formulation reported by Fuller *et al.*[40],

$$D_{j,q} = \frac{10^{-3}T[K]^{1.75}(M_i[\mathrm{g\ mol^{-1}}]^{-1} + M_i[\mathrm{g\ mol^{-1}}]^{-1})^{0.5}}{p_G[\mathrm{atm}]\left(v_{p,j}^{0.33} + v_{p,q}^{0.33}\right)^2} \tag{47}$$

$$D_j^{\mathrm{m}} = \frac{1 - \omega_{\mathrm{i}}}{\sum_{n \neq j} \frac{y_n}{D_{j,n}}} \tag{48}$$

Where $v_{p,j}$ is the diffusion volume of species j. The convective velocity of the gas-phase ($\boldsymbol{u_G}$) in the CL pores was determined using Darcy's law and the Carman-Kozeny equation to account for flow in porous media,

$$\boldsymbol{u_G} = -\frac{\kappa_{sat}^0 \kappa_{rG}}{\mu_G} \frac{(1-\varepsilon_S)^3}{(\varepsilon_S)^2} \nabla p_G \tag{49}$$

The relative permeability (κ_{rG}) of the gas-phase was estimated based on a cubic dependency on water saturation,

$$\kappa_{rg} = (1-S)^3 \tag{50}$$

The final equation used to solve the governing mass balances for the gas-phase is the summation of mass fractions,

$$\sum_j \omega_j = 1 \tag{51}$$

4.5 CO_2 phase transfer and solubility

The rate of phase-transfer (PT) for CO_2 ($R_{PT,\mathrm{CO_2}}$) occurring at the gas/ionomer interface was calculated as follows,

$$R_{PT,\mathrm{CO_2}} = a_v k_{GL,\mathrm{CO_2}} M_{\mathrm{CO_2}} \varepsilon_I \left(\mathrm{H_{CO_2}} p_G y_{\mathrm{CO_2}} - c_{\mathrm{CO_2}}\right) \tag{52}$$

where H_{CO_2} is the Henry's Law coefficient for CO_2 dissolved in the electrolyte, c_{CO_2} is the concentration of dissolved CO_2, M_{CO_2} is the molar mass of CO_2, k_{GL,CO_2} is the mass-transfer coefficient, which was obtained from experimental data by Yang *et al.*[41], and y_{CO_2} is the mole fraction of CO_2 in the gas-phase. The reduction in CO_2 solubility observed at high salt concentrations (i.e., the "salting-out" effect) was accounted for using the Sechenov formulation with parameters obtained from Weisenberger and Schumpe (**Table S6**)[42],

$$H_{CO_2} = 10^{-\sum_i (h_{CO_2}+h_i)c_i} H^0_{CO_2} \tag{53}$$

Where h_i represents the solubility coefficient for the different salt species in solution. The nominal Henry's Law coefficient for CO_2 dissolved in water (in units mM atm^{-1}) is given as,

$$H^0_{CO_2} = 34 \exp(2400(\frac{1}{T} - \frac{1}{298\ \mathrm{K}})) \tag{54}$$

CO and H_2 were assumed to be insoluble in the ionomer and generated directly in the gas phase, therefore the rate of CO and H_2 generation in the gas-phase were calculated using Faraday's Law,

$$R_{PT,j\neq CO_2} = \frac{a_v s_{j,k} |i_k|}{n_k F} \tag{55}$$

4.6 Water chemical potential and transport

The ionomer-phase in the MEA is considered to be continuous between the anode and cathode catalyst layers. Therefore, liquid water is transported across the membrane by dissolving in the ionomer-phase of the anode catalyst layer and transporting across the membrane to the cathode catalyst layer according to the chemical potential gradient, which is defined as

$$\mu_w = RT\ln(a_w) + V_{\mathrm{m},w}(p_{L,M} - p_{L,ref}) \tag{56}$$

where a_w is the activity of water in the ionomer, $p_{L,M}$ is the pressure of liquid water in the membrane, $V_{\mathrm{m},w}$ is the molar volume of water (18 mL mol^{-1}), and $p_{L,ref}$ is the reference liquid pressure (1 atm). Concentrated-solution theory was considered for water transport due to the need to account for electroosmosis. Therefore, the equations that describes water conservation and flux are given by,

$$\boldsymbol{\nabla} \cdot \boldsymbol{n_w} = R_{k,w} \tag{57}$$

$$\boldsymbol{n_w} = -\alpha_w \boldsymbol{\nabla}\mu_w + \sum_i \zeta_i \boldsymbol{n_i} \tag{58}$$

Where $\boldsymbol{n_w}$ is the molar flux of water, μ_w is the water chemical potential, and $R_{k,w}$ is the net molar rate of water generation by electrochemical and buffer reactions and phase-transfer phenomena. α_w is the water transport coefficient, which was implemented as a function of water activity as per experimental measurements by Petrovick *et al.*[43] (**Figure S20**). The first term in Eq. (58) describes the transport of water under chemical-potential-gradient driving force, analogous to the relationship between the diffusion coefficient and concentration gradient for Fickian diffusion processes. ζ_i is the electro-osmotic coefficient for species i, which was determined experimentally[43]

$$\zeta_i = \frac{\boldsymbol{n_{H_2O}}}{\boldsymbol{n_i}} \tag{59}$$

Correspondingly, the second term in Eq. (58) is associated with electroosmotic driving forces that couple water transport to the transport of ions in the electrolyte.

The net electroosmotic coefficient (β) relates the amount of water transported relative to the amount of water consumed by electrochemical reactions and is given as,

$$\beta = \frac{\boldsymbol{n_{H_2O}}}{\boldsymbol{i}/F} \tag{60}$$

The rate at which liquid water transfers from the liquid to the ionomer phase (R_{LI}, w) is governed by the difference in pressure between the two phases,

$$R_{LI,\mathrm{w}} = a_v k_{MT,\mathrm{L}}\left(p_L - p_{L,M}\right) \tag{61}$$

where $k_{MT,\mathrm{L}}$ is the interfacial mass transfer coefficient for liquid water (**Table S6**). The rate of water transport from the gas-phase to the ionomer-phase is given by,

$$R_{GI,\mathrm{w}} = a_v k_{MT,\mathrm{V}}\left(\frac{\mathrm{RH}}{100} - a_w\right) \tag{62}$$

where RH is the relative humidity and $k_{MT,\mathrm{V}}$ is the interfacial mass transfer coefficient for water vapor (**Table S6**). These phase-transfer source terms are used in the momentum balances for the liquid- and gas-phases,

$$Q_G = -\sum_j R_{PT,j} MW_j - R_{GI,w} MW_w \tag{63}$$

$$Q_L = -R_{LI,w} MW_w + R_{GL,w} MW_w \tag{64}$$

The opposite signs for the mass source terms ensures that the amount of water that leaves one phase is exactly equal to the water that enters the other phase.

4.7 Boundary Conditions

As seen in **Figure 1b**, the far left of the simulation domain represents the interface between the anode porous-transport layer and the flow field/current collector. Here, Dirichlet boundary conditions are used to describe the solid-phase potential, water chemical potential, and pressure of liquid-water and gas in the channel,

$$V_{x=0} = 0\ \text{V} \tag{65}$$

$$\mu_{w,x=0} = 0\ \frac{\text{J}}{\text{mol}} \tag{66}$$

$$p_{L,x=0} = 1\ \text{bar} \tag{67}$$

$$p_{G,x=0} = 1\ \text{bar} \tag{68}$$

The boundary condition described by (65) implies that the anode is at a reference potential of 0 V vs. the standard hydrogen electrode (SHE). The boundary conditions described by (66) and (67) imply that the water activity is 1 and that the electrolyte is at ambient pressure, respectively (*i.e.*, a liquid electrolyte feed is used).

The flux of ions and dissolved CO_2 to and from the anode flow field is given by a mass-transfer correlation,

$$\boldsymbol{n_{i\neq w,x=0}} = k_{MT,i}(c_{i,bulk} - c_{i,x=0}) \tag{69}$$

where the mass-transfer coefficients are given by a flat-plate correlation describing convective mass transfer,

$$k_{MT,i\neq w} = 0.664\frac{D_j}{L_{elect.}}\mathrm{Re}_i^{1/2}\mathrm{Sc}_i^{1/3} \tag{70}$$

where $\mathrm{Re_i}$ and $\mathrm{Sc_i}$ are the Reynold's and Shmidt numbers for species i and $L_{elect.}$ is the characteristic electrode length. Convective transport of gas across the membrane is assumed to be negligible. Water transport across the membrane is driven only by diffusion and electro-osmosis within the hydrophilic domains of the polymer because there is no forced convection within these mesoscale channels. Therefore, the velocity of both gas and liquid phases at the membrane/electrode interfaces is assumed to be 0 m s^{-1} in the momentum balance equations,

$$\boldsymbol{u_{L,x=200,250\ \mu m}} = 0 \tag{71}$$

$$\boldsymbol{u_{G,x=200,250\ \mu m}} = 0 \tag{72}$$

Dirichlet boundary conditions are used for the gas-phase mass conservation equations to represent the use of 100% humidified CO_2 at the interface between the carbon GDL/cathode flow field and the use of N_2 as a carrier gas at the anode PTL/anode flow field,

$$\omega_{j,x=585\ \mu m} = \omega_{j,bulk} \tag{73}$$

$$\omega_{j,x=0\ \mu m} = \omega_{j,bulk} \tag{74}$$

A no-flux boundary condition was used for the chemical potential of water at the cathode

CL/GDL interface,

$$\left.\frac{d\mu_w}{dx}\right|_{x=260\ \mu m} = 0 \tag{75}$$

Finally, chronoamperometry experiments were simulated by setting the V_{cell} at the catalyst-layer/gas-diffusion-layer interface,

$$V_{x=360\ \mu m} = V_{cell} \tag{76}$$

The boundary condition described by (76) implies that the imposed potential at the cathode boundary in the model is equivalent to the electrolytic cell potential applied in the experiment, whereas (65) specifies the anode as the ground. The equations that comprise the model were solved using the MUMPS solver in COMSOL with 14000 elements and a relative error of 1 x 10^{-4}.

4.8 Applied-voltage breakdown, Faradaic efficiency for CO, and CO_2 utilization

The total cell voltage was decomposed into the thermodynamic potential and overpotentials using power-loss analysis first described by Secanell *et al.*[44, 45] The thermodynamic potential of the anode ($\Delta V_{therm,anode}$) and cathode reactions ($\Delta V_{therm,cathode}$) are,

$$\Delta V_{therm,anode} = \frac{1}{L_{aCL}} \int_{aCL} \frac{i_{OER}\left(U^0_{OER} - \frac{2.303RT}{F}\mathrm{pH}\right)}{i_{total}}\ \mathrm{dx} \tag{77}$$

$$\Delta V_{therm,cathode} = \frac{1}{L_{cCL}} \int_{cCL} \frac{i_{HER}(U^0_{HER} - \frac{2.303RT}{F}\text{pH})}{i_{total}}\ \text{dx} + \frac{1}{L_{cCL}} \int_{cCL} \frac{i_{COER}(U^0_{COER} - \frac{2.303RT}{F}\text{pH})}{i_{total}}\ \text{dx} \quad (78)$$

The overpotentials associated with OER, HER, and CO2R are given as,

$$\Delta V_{OER} = \frac{1}{L_{aCL}} \int_{aCL} \frac{\eta_{OER} i_{OER}}{i_{total}}\ \text{dx} \quad (79)$$

$$\Delta V_{HER} = \frac{1}{L_{cCL}} \int_{cCL} \frac{\eta_{HER} i_{HER}}{i_{total}}\ \text{dx} \quad (80)$$

$$\Delta V_{COER} = \frac{1}{L_{cCL}} \int_{cCL} \frac{\eta_{COER} i_{COER}}{i_{total}}\ \text{dx} \quad (81)$$

The voltage drops due to ionic (ΔV_{ionic}) and ($\Delta V_{electrical}$) electrical Ohmic losses are,

$$\Delta V_{ionic} = \int_{x=0\ \mu m}^{x=360\ \mu m} \frac{\boldsymbol{i_l} \cdot \nabla \phi_l}{i_{total}}\ \text{dx} \quad (82)$$

$$\Delta V_{electrical} = \int_{x=0\ \mu m}^{x=360\ \mu m} \frac{\boldsymbol{i_s} \cdot \nabla \phi_s}{i_{total}}\ \text{dx} \quad (83)$$

The Faradaic efficiency for CO (FE_{CO}) and CO_2 utilization efficiency are,

$$\text{FE}_{\text{CO}} = \frac{i_{COER}}{i_{total}} \quad (84)$$

$$\text{CO}_2\text{utilization} = \frac{\frac{i_{COER}}{n_{CO}F}}{R_{\text{PT,CO}_2,aCL}} \quad (85)$$

Where the numerator of Eq. (85) represents the amount of CO formed and the denominator represents the amount of CO_2 that reacts to form (bi)carbonates and crosses the membrane to the

anode where it reconverts and is released as CO_2.

4.9 Experimental Methods

4.9.1 Membrane-electrode-assembly design

The Ag cathode ink was prepared by mixing Ag/C particles (i.e., 20% Ag on Vulcan XC-72 carbon support, Premetek®), Sustainion® ionomer (5% in ethanol, Dioxide Materials®), water (Milli-Q®, 18 mΩ), and n-propanol (Sigma-Aldrich®). The Ir-anode catalyst ink was composed of IrO_2 nanoparticles (Tanaka®, SA=100), Sustainion® ionomer (at a loading of 11.6 wt.-%), water, n-propanol, and ethanol (Sigma-Aldrich®). The inks were ultrasonicated (Symphony® Sonicator) for 30 min.

The cathode electrode substrate consisted of a microporous layer (MPL) covering a gas-diffusion layer made of carbon fibers and 5 wt.-% polytetrafluoroethylene (PTFE) with a total composite porosity of 0.52 (Sigracet® 39BC). The anode electrode substrate was a proprietary mesoporous titanium (Ti) porous-transport layer provided by NEL Hydrogen®. Before deposition, both electrode substrates were cleaned with ultra-pure nitric acid in order to remove electrochemically-active trace impurities. Catalyst inks were then spray-coated onto the cathode and anode substrates using an ultrasonic spray coater (Sono-Tek® Exactacoat). For each electrode, the spray coating time was adjusted to achieve the desired loading.

The anode and cathode gas-diffusion electrodes were placed across a 50 μm-thick hydrated Sustainion® X37-50 Grade RT membrane (Dioxide Materials®) to form the MEA. The MEA was operated in a 5 cm^2 commercial cell (Fuel Cell Technologies®). A torque wrench was used to tighten each cell bolt to 40 in-lb and 10-mil thick PTFE gaskets (Fuel Cell Technologies®)

were used on each gas channel to ensure reproducible and uniform compression across the MEA and to prevent leakage. The cell was then connected to a potentiostat fitted with a 10A booster (Bio-Logic®) and heating elements to enable operation at 50°C.

4.9.2 Materials characterization

Powder x-ray diffraction (XRD) patterns of the Ag/C particles and their carbon support (Vulcan XC-72) were recorded using a MiniFlex 6G X-ray diffractometer (Rigaku) equipped with a Cu $K\alpha$ radiation (wavelength = 1.5418 Å; **Figure S21**). A tube voltage of 40 kV and tube current of 15 mA were used. The PXRD scanning rate was 5° min^{-1} in the scan range of 2θ from 2 to 80°. A FEI ThemIS 60-300 (Thermo Fisher Scientific) transmission electron microscope was used to acquire TEM, scanning transmission electron microscopy (STEM) and energy dispersive X-ray spectroscopy (EDS) data of the Ag/C and the ionomer-coated Ag/C (**Figure S18**). The microscope was operated at an accelerating voltage of 300 kV and is equipped with an image aberration corrector and a Bruker SuperX energy dispersive x-ray spectroscopy detector. A Ceta2 CMOS camera and a high-angle annular dark field detector were used for TEM and STEM imaging, respectively. Based on this analysis, the average particle radius was estimated to be 25 nm.

4.9.3 Electrochemical measurements

The CO_2 entering the cathode compartment was humidified by bubbling it through deionized water (Milli-Q®, 18 mΩ) maintained at 50°C using a hot-water bath. Cesium bicarbonate ($CsHCO_3$) (Sigma-Aldrich®) at 50°C was fed behind the anode as the MEA exchange solution. The cathode feed flow rate was set to or above 200 mL min^{-1} of humidified CO_2 (measured using a mass-flow controller (Alicat Scientific®)). 1 M $CsHCO_3$ was delivered to anode

at a flow rate of 25 mL min^{-1} using a peristaltic pump (Masterflex®). Flowrates of the cathode and anode product gases were measured using a mass-flow meter (MFM) (Alicat Scientific®) downstream of the electrolyzer.

The cell was first held at open circuit for 30 to 60 min to ensure thermal uniformity and complete hydration of the cell membrane and the ionomer in the catalyst layers. Chronoamperometry (constant voltage) electrolysis was performed together with in-line gas-chromatography (GC) analysis (SRI Instruments®) using both a flame-ionization detector and a thermal-conductivity detector. A polarization curve was obtained, with each voltage step being held for at least 30 min. For each voltage step, the reported current density was averaged over the last 15 min. Two GC samples were taken per electrode: the measured CO and H_2 product concentrations, the corresponding current density, and the outlet flow rate were used to determine the partial current densities for each product at each voltage step. The CO_2 crossover flux through the CO2R electrolyzer was determined from GC measurements by flowing N_2 gas through the headspace of the 1 M $CsHCO_3$ anolyte reservoir. A photograph of the final assembly is shown in **Figure S22**.

5. Acknowledgements

The authors acknowledge Alex J. King for graphic design and interpretation of the CO2R reorganization energy. Transmission electron microscopy (TEM) and powder X-ray diffraction (PXRD) were performed by Daewon Lee in Prof. Haimei Zheng's group, supported by the U.S. Department of Energy, Office of Science, Office of Basic Energy Sciences (BES), Materials Sciences and Engineering Division under Contract No. DE-AC02-05-CH11231 within the in-situ TEM

program (KC22ZH). The authors gratefully acknowledge Lawrence Berkeley National Laboratory's Laboratory Directed Research and Development (LDRD) Grant for funding. This material is also partially based upon work performed by support from the DOE EERE Bioenergy Technologies Office under Contract Number DE-AC02-05CH11231. EWL would like to acknowledge support from the National Science and Engineering Research Council (NSERC) postdoctoral fellowship. J.C.B. was supported in part by a fellowship award under contract FA9550-21-F-0003 through the National Defense Science and Engineering Graduate (NDSEG) Fellowship Program, sponsored by the Army Research Office (ARO).

6. Competing interests statement

The authors declare no competing or financial interests.

7. Data availability

The experimental data is available upon request.

8. Code availability

The COMSOL code is available upon request. Instructions regarding downloading COMSOL and running simulations can be found on the COMSOL website (https://doc.comsol.com/6.2/docserver/#!/com.comsol.help.comsol/helpdesk/helpdesk.html).

9. Nomenclature

Roman

a_i	Activity of species *i*
a_v	Volumetric specific surface area (m^{-1})
c_i	Concentration of species *i* (M)

D_i	Diffusivity of species i ($m^2\ s^{-1}$)
F	Faraday constant ($C\ mol^{-1}$)
H_{CO_2}	Henry's constant for CO_2 (mM/atm)
h_i	Solubility parameter
IEC	Ion Exchange capacity ($mmol\ g^{-1}$)
$\boldsymbol{i}$	Current density ($mA\ cm^{-2}$)
J_j	Mass flux of species j ($kg\ m^{-2}\ s^{-1}$)
k_B	Boltzmann constant ($J\ K^{-1}$)
K_n	Equilibrium constant in reaction n
k_n	Forward rate constant of reaction n ($m^3\ s^{-1}\ mol^{-1}$)
$k_{0,CO}$	Pre-exponential factor for CO2R ($mA\ cm^{-2}$)
L	Length (m)
M_i	Molar mass of species i ($g\ mol^{-1}$)
$\boldsymbol{n_i}$	Molar flux of species i ($mol\ m^{-2}\ s^{-1}$)
n_k	Number of electrons transferred in reaction k
p	Pressure (atm)
Q	Mass generation/consumption term ($kg\ m^{-3}\ s^{-1}$)
q	Membrane tortuosity parameter
R	Ideal gas constant ($J\ mol^{-1}\ K^{-1}$)
$R_{B,i}$	Mole generation/consumption for species i ($mol\ m^{-3}\ s^{-1}$)
$R_{PT,i/j}$	Molar rate of phase-transfer for species i or j ($mol\ m^{-3}\ s^{-1}$)
r_p	Catalyst particle radius (m)
S	Liquid water saturation
$s_{i,n}$	Stoichiometric coefficient of species i in reaction n
T	Temperature (K)
$\boldsymbol{u}$	Mass averaged velocity ($m\ s^{-1}$)

V	Voltage (V)
$\overline{\mathrm{V}}$	Molar volume of water (m^3 mol^{-1})
x	1-dimensional position variable (m)
x_w	Water volume fraction
y_i	Mole fraction of gaseous species *i*
z_i	Charge of ion *i*

Greek

$\alpha_{a,k}$	Transfer coefficient of anodic reaction *k*
$\alpha_{c,k}$	Transfer coefficient of cathodic reaction *k*
α_{CIMD}	Fraction of protonated imidazolium groups
α_w	Water transport coefficient (mol J^{-1} cm^{-1} s^{-1})
ε_k	Volume fraction of phase *k*
ζ_i	Electroosmotic drag coefficient of species *i*
η_k	Overpotential of reaction *k* (V)
λ	Water content
λ_{reorg}	Reorganization energy (eV)
μ	Viscosity (Pa s)
μ_w	Chemical potential of water (J mol^{-1})
$\nu_{p,j}$	Diffusion volume of gaseous species *j*
σ	Electric conductivity (S m^{-1})
ρ	Density (g cm^{-3})
Φ_w	Water volume fraction
ϕ	Potential (V)
ψ	Ratio between species-solvent and species-membrane interactions
ω_i	Mass fraction of gaseous species *i*

Subscript

cap	Capillary
CT	Charge-transfer
eff	Effective
G	Gas-phase
I	Ionomer-phase
i	Ionic species
j	Gaseous species
L	Liquid-phase
M	Membrane
PT	Phase-transfer
q	Other gaseous species
reorg	Reorganization energy
s	Solid phase
sat	Saturated value
ref	Reference value
w	Value in water

Superscript

eff	Effective
K	Knudsen
m	Molecular

0	Intrinsic value or standard state

Acronyms

AEM	Anion exchange layer
aPTL	Anode porous transport layer
aCL	Anode catalyst layer
cCL	Cathode catalyst layer
cGDL	Cathode gas diffusion layer
CO2R	CO_2 reduction
GC	Gas chromatography
HER	Hydrogen evolution reaction
MEA	Membrane electrode assembly
MHC	Marcus-Hush-Chidsey
MPL	Microporous layer
STEM	Scanning transmission electron microscopy
TEM	Transmission electron microscopy
XRD	X-ray diffraction
EDS	Energy-dispersive X-ray spectroscopy

10. References

1. Izadi P, Harnisch F. Microbial vertical bar electrochemical CO2 reduction: To integrate or not to integrate? *Joule* 2022, **6**(5)**:** 935-940.

2. De Luna P, Hahn C, Higgins D, Jaffer SA, Jaramillo TF, Sargent EH. What would it take for renewably powered electrosynthesis to displace petrochemical processes? *Science* 2019, **364**(6438)**:** 350-+.

3. Somoza-Tornos A, Guerra OJ, Crow AM, Smith WA, Hodge BM. Process modeling, techno-economic assessment, and life cycle assessment of the electrochemical reduction of CO2: a review. *Iscience* 2021, **24**(7).

4. Salvatore D, Berlinguette CP. Voltage Matters When Reducing CO2 in an Electrochemical Flow Cell. *Acs Energy Lett* 2020, **5**(1)**:** 215-220.

5. Jouny M, Luc W, Jiao F. General Techno-Economic Analysis of CO2 Electrolysis Systems. *Ind Eng Chem Res* 2018, **57**(6)**:** 2165-2177.

6. Endrodi B, Samu A, Kecsenovity E, Halmagyi T, Sebok D, Janaky C. Operando cathode activation with alkali metal cations for high current density operation of water-fed zero-gap carbon dioxide electrolysers. *Nat Energy* 2021, **6**(4)**:** 439-448.

7. Kutz RB, Chen QM, Yang HZ, Sajjad SD, Liu ZC, Masel IR. Sustainion Imidazolium-Functionalized Polymers for Carbon Dioxide Electrolysis. *Energy Technol-Ger* 2017, **5**(6)**:** 929-936.

8. Jeng E, Jiao F. Investigation of CO2 single-pass conversion in a flow electrolyzer. *React Chem Eng* 2020, **5**(9)**:** 1768-1775.

9. Blommaert MA, Subramanian S, Yang K, Smith WA, Vermaas DA. High Indirect Energy Consumption in AEM-Based CO(2) Electrolyzers Demonstrates the Potential of Bipolar Membranes. *ACS Appl Mater Interfaces* 2022, **14**(1)**:** 557-563.

10. da Cunha SR, J. Maximizing single-pass conversion does not result in practical readiness for CO2 reduction electrolyzers. *Nat Commun* 2023, **14:** 5513.

11. Xie K, Miao RK, Ozden A, Liu SJ, Chen Z, Dinh CT*, et al.* Bipolar membrane electrolyzers enable high single-pass CO2 electroreduction to multicarbon products. *Nat Commun* 2022, **13**(1).

12. Disch J, Ingenhoven S, Vierrath S. Bipolar Membrane with Porous Anion Exchange Layer for Efficient and Long-Term Stable Electrochemical Reduction of CO2 to CO. *Advanced Energy Materials* 2023, **13**(38)**:** 2301614.

13. Lees EW, Mowbray BAW, Parlane FGL, Berlinguette CP. Gas diffusion electrodes and membranes for CO2 reduction electrolysers. *Nat Rev Mater* 2022, **7**(1)**:** 55-64.

14. Salvatore DA, Gabardo CM, Reyes A, O'Brien CP, Holdcroft S, Pintauro P*, et al.* Designing anion exchange membranes for CO2 electrolysers. *Nat Energy* 2021, **6**(4)**:** 339-348.

15. Weng LC, Bell AT, Weber AZ. Towards membrane-electrode assembly systems for CO2 reduction: a modeling study. *Energ Environ Sci* 2019, **12**(6)**:** 1950-1968.

16. Blake JW, Padding JT, Haverkort JW. Analytical modelling of CO2 reduction in gas-diffusion electrode catalyst layers. *Electrochimica Acta* 2021, **393**.

17. Weng LC, Bell AT, Weber AZ. Modeling gas-diffusion electrodes for CO2 reduction. *Phys Chem Chem Phys* 2018, **20**(25)**:** 16973-16984.

18. Loffelholz M, Osiewacz J, Luken A, Perrey K, Bulan A, Turek T. Modeling electrochemical CO2 reduction at silver gas diffusion electrodes using a TFFA approach. *Chem Eng J* 2022, **435**(Pt 2).

19. Romiluyi O, Danilovic N, Bell AT, Weber AZ. Membrane-electrode assembly design parameters for optimal CO2 reduction. *Electrochemical Science Advances* 2023, **3**(1)**:** e2100186.

20. Brown SMO, M.; Hsiao, Y. W.; Yuriy, R-L.; Surendranath, Y.; Bazant, M. Z.; Brushett, F. . Electron transfer limitation in carbon dioxide reduction revealed by data-driven Tafel analysis. *ChemRxiv* 2021.

21. Corpus KRM, Bui JC, Limaye AM, Pant LM, Manthiram K, Weber AZ*, et al.* Coupling covariance matrix adaptation with continuum modeling for determination of kinetic parameters associated with electrochemical CO2 reduction. *Joule* 2023, **7**(6).

22. Henstridge MC, Laborda E, Rees NV, Compton RG. Marcus-Hush-Chidsey theory of electron transfer applied to voltammetry: A review. *Electrochimica Acta* 2012, **84:** 12-20.

23. Bazant MZ. Unified quantum theory of electrochemical kinetics by coupled ion-electron transfer. *Faraday Discuss* 2023.

24. Reddy PN, Reddy MHP, Pierson JF, Uthanna S. Characterization of Silver Oxide Films Formed by Reactive RF Sputtering at Different Substrate Temperatures. *ISRN Optics* 2014, **2014:** 684317.

25. Vass A, Endrodi B, Samu GF, Balog A, Kormanyos A, Cherevko S*, et al.* Local Chemical Environment Governs Anode Processes in CO2 Electrolyzers. *Acs Energy Lett* 2021, **6**(11)**:** 3801-3808.

26. Wheeler DG, Mowbray BAW, Reyes A, Habibzadeh F, He JF, Berlinguette CP. Quantification of water transport in a CO

electrolyzer. *Energ Environ Sci* 2020, **13**(12)**:** 5126-5134.

27. Petrovick JG, Kushner DI, Goyal P, Kusoglu A, Radke CJ, Weber AZ. Electrochemical Measurement of Water Transport Numbers in Anion-Exchange Membranes. *J Electrochem Soc* 2023, **170**(11)**:** 114519.

28. Dunwell M, Lu Q, Heyes JM, Rosen J, Chen JGG, Yan YS*, et al.* The Central Role of Bicarbonate in the Electrochemical Reduction of Carbon Dioxide on Gold. *J Am Chem Soc* 2017, **139**(10)**:** 3774-3783.

29. Hashiba H, Weng LC, Chen YK, Sato HK, Yotsuhashi S, Xiang CX*, et al.* Effects of Electrolyte Buffer Capacity on Surface Reactant Species and the Reaction Rate of CO

in Electrochemical CO

Reduction. *J Phys Chem C* 2018, **122**(7)**:** 3719-3726.

30. Luo XY, Kushner DI, Kusoglu A. Anion exchange membranes: The effect of reinforcement in water and electrolyte. *J Membrane Sci* 2023, **685**.

31. Andersen MB, van Soestbergen M, Mani A, Bruus H, Biesheuvel PM, Bazant MZ. Current-Induced Membrane Discharge. *Physical Review Letters* 2012, **109**(10)**:** 108301.

32. Zenyuk IV, Das PK, Weber AZ. Understanding Impacts of Catalyst-Layer Thickness on Fuel-Cell Performance via Mathematical Modeling. *J Electrochem Soc* 2016, **163**(7)**:** F691-F703.

33. Bui JC, Lucas É, Lees EW, Liu AK, Atwater HA, Xiang C*, et al.* Analysis of bipolar membranes for electrochemical CO2 capture from air and oceanwater. *Energ Environ Sci* 2023, **16**(11)**:** 5076-5095.

34. Weng LC, Bell AT, Weber AZ. A systematic analysis of Cu-based membrane-electrode assemblies for CO(2)reduction through multiphysics simulation. *Energ Environ Sci* 2020, **13**(10)**:** 3592-3606.

35. Khan SUM, Bockris JO. Electronic States in Solution and Charge-Transfer. *J Phys Chem-Us* 1983, **87**(14)**:** 2599-2603.

36. Zeng Y, Smith RB, Bai P, Bazant MZ. Simple formula for Marcus-Hush-Chidsey kinetics. *J Electroanal Chem* 2014, **735:** 77-83.

37. Smith RB, Bazant MZ. Multiphase Porous Electrode Theory. *J Electrochem Soc* 2017, **164**(11)**:** E3291.

38. Singh MR, Goodpaster JD, Weber AZ, Head-Gordon M, Bell AT. Mechanistic insights into electrochemical reduction of CO2 over Ag using density functional theory and transport models. *P Natl Acad Sci USA* 2017, **114**(42)**:** E8812-E8821.

39. Peng J, Roy AL, Greenbaum SG, Zawodzinski TA. Effect of CO2 absorption on ion and water mobility in an anion exchange membrane. *Journal of Power Sources* 2018, **380:** 64-75.

40. Fuller EN, Schettle PD, Giddings JC. A New Method for Prediction of Binary Gas-Phase Diffusion Coeffecients. *Ind Eng Chem* 1966, **58**(5)**:** 19-+.

41. Yang ZM, Li D, Xing L, Xiang H, Xuan J, Cheng SA*, et al.* Modeling and Upscaling Analysis of Gas Diffusion Electrode-Based Electrochemical Carbon Dioxide Reduction Systems. *Acs Sustain Chem Eng* 2021, **9**(1)**:** 351-361.

42. Weisenberger S, Schumpe A. Estimation of gas solubilities in salt solutions at temperatures from 273 K to 363 K. *Aiche J* 1996, **42**(1)**:** 298-300.

43. Petrovick JGK, D. I.; Goyal, P.; Kusoglu, A.; Radke, C. J.; Weber, A. Z. Electrochemical Measurement of Water Transport Numbers in Anion-Exchange Membranes. *J Electrochem Soc* 2023, **170**(114519).

44. Kosakian A, Urbina LP, Heaman A, Secanell M. Understanding single-phase water-management signatures in fuel-cell impedance spectra: A numerical study. *Electrochimica Acta* 2020, **350**.

45. Gerhardt MR, Pant LM, Bui JC, Crothers AR, Ehlinger VM, Fornaciari JC*, et al.* Method-Practices and Pitfalls in Voltage Breakdown Analysis of Electrochemical Energy-Conversion Systems. *J Electrochem Soc* 2021, **168**(7).